Sea-Spray-Generation Dependence on Wind and Wave Combinations: A Laboratory Study

William Bruch, Jacques Piazzola, Hubert Branger, Alexander M J van Eijk, Christopher Luneau, Denis Bourras, Gilles Tedeschi

Boundary-Layer Meteorology manuscript No.
(will be inserted by the editor)

Sea Spray Generation Dependence on Wind and Wave Combinations : A Laboratory Study

William Bruch · Jacques Piazzola · Hubert Branger · Alexander M. J. van Eijk · Christopher Luneau · Denis Bourras · Gilles Tedeschi

Received: DD Month 2020 / Accepted: DD Month YEAR

Abstract This paper investigates the effect of interacting winds and waves on the surface sea spray generation flux. To this end, the Marine Aerosol Tunnel Experiment (MATE2019) was conducted at the OSU-Pytheas large wind-wave tunnel facility at Luminy, Marseille (France), in June-July 2019. A unique range of air-sea boundary conditions was generated by configuring the laboratory with four types of wave forcing and five wind speeds ranging from 8 to 20 m s^{-1}. The configurations included both young and developed

William Bruch, Jacques Piazzola and Gilles Tedeschi
Mediterranean Institute of Oceanography (MIO - UMR 7294), Université de Toulon, France
E-mail: william.bruch@mio.osupytheas.fr (✉) and jacques.piazzola@mio.osupytheas.fr (✉)

Hubert Branger
IRPHE, CNRS, Aix-Marseille Université, ECM, France.

Alexander van Eijk
TNO, Netherlands − LHEEA (UMR 6598), École Centrale de Nantes, France

Christopher Luneau
CNRS, OSU-Pytheas, Aix-Marseille Université, France.

Denis Bourras
Mediterranean Institute of Oceanography (MIO - UMR 7294), Aix-Marseille Université, France.

waves spanning a wave age (defined in terms of phase speed and friction velocity) range between 1.3 and 9.5. Sea spray concentrations were measured over the 0.1-47.5 μm radius range at different heights above water, and a flux-profile method using Monin and Obukhov (1954) theory allowed to estimate the sea spray generation flux from concentration profiles. Results show that the flux increases for increased wind-induced wave breaking, and the highest flux is found for steep and heavily-breaking wind-forced waves. Scaling analysis shows that the sea spray generation is best correlated with the wave slope variance ($< S^2 >$) for larger droplets (20 μm and above, assumed predominantly spume droplets generated by surface tearing). For smaller droplets (7-20 μm, presumed predominantly jet droplets generated by bubble bursting) highest correlation is found with a non-dimensional number combining $< S^2 >$ and the friction velocity cubed u_*^3. This is reflected in the formulation of two wave state dependent sea spray generation functions (SSGFs), each valid for wind speeds 12-20 m s^{-1} and droplet radii 3-35 μm, thereby covering both jet and spume droplet production.

Keywords Sea spray generation · Air-sea interaction · Wave slope variance · Friction velocity cubed

1 Introduction

Sea spray aerosols formed by the interaction between air and water represent a major component of the natural aerosol mass (Jaenicke, 1984; Yoon et al., 2007) with a major role in the Earth radiation budget (Mallet et al., 2003; Mulcahy et al., 2008). In turn, the light scattering by sea spray aerosols is an important factor in the context of climate change (Lewis et al., 2004). Sea spray

also has a significant impact on air quality, particularly in coastal regions where anthropogenic emissions are high (Piazzola et al., 2016; Johansson et al., 2019). However, it remains difficult to numerically model these effects. Significant predictive uncertainties remain for sea spray aerosol in numerical models with significant biases observed for commonly used emission schemes (Tsyro et al., 2011; Chen et al., 2016; Neumann et al., 2016). Therefore, sea spray aerosol generation and subsequent transport in the atmosphere models need to be improved (Canepa and Builtjes, 2017).

Sea spray can be produced both directly and indirectly from the water surface. Indirect generation is associated with the relatively small bubble-mediated jet and film droplets produced by wave breaking, effective for wind speeds around 4 m s^{-1} and above (Blanchard, 1963; Spiel, 1994). The transition from film to jet droplet dominance is thought to occur at radii 2 - 4 μm (Cipriano and Blanchard, 1981; Woolf, 1997) with jet droplets dominating over the 2 - 20 μm range and sometimes reaching 50 μm or more (Newitt, 1954; Andreas, 1998). The direct sea spray generation mechanisms activated at wind speeds higher than 10 - 12 m s^{-1} (Monahan et al., 1986; Andreas et al., 2010) consist of surface-tearing of larger (radius $r > 20$ μm) spume droplets that are directly ejected into the air flow.

The direct generation mechanisms have proven to be elusive. Anguelova et al. (1999) noted the tearing of spume drops at the wave crests by the wind, and found spume droplet generation to be strongly related to the whitecap coverage. On a microphysical scale the bag breakup of small canopies of water produced by wind surface friction at the wave crests is a potential mechanism for spume droplet generation (Mueller and Veron, 2009; Veron et al., 2012; Troitskaya et al., 2018). All in all, little is known about the generation of particles of radii > 20 μm (Veron et al., 2012; Veron, 2015). A better pa-

rameterization of the droplet generation flux and transport over this range is urgently needed, since a major portion of the total volume of sea spray droplets is thought to be within the 10-200 μm radius range, as stressed by authors such as Andreas (1992).

The sea spray flux or sea spray generation function (SSGF) is known to depend on numerous environmental parameters such as the wind and wave fields (De Leeuw, 1986; Iida et al., 1992; Smith et al., 1993), the sea surface temperature (Mårtensson et al., 2003), and the composition and salinity of the seawater (Sellegri et al., 2006; Mehta et al., 2019). Although wind speed alone was traditionally used to parameterize the aerosol generation - cf. the SSGFs of Monahan et al. (1986); Smith et al. (1993); Andreas (1998) - there is increasing evidence that this is not sufficiently accurate, and additional environmental conditions have to be taken into account, wave parameters especially. Various authors have also considered scaling droplet generation with non-dimensional numbers such as wave age (Lafon et al., 2007; Laussac et al., 2018), or the windsea Reynolds number R_B (Zhao et al., 2006; Ovadnevaite et al., 2014; Troitskaya et al., 2018). The wave age is defined as the ratio between the wave phase velocity c_p and a wind parameter (for example the wind friction velocity u_*), and is generally used to describe wave-field developement and wave-wind equilibrium. R_B, first introduced by Toba and Koga (1986) as $u_*^2/(\nu_a \omega_p)$ with the air kinetic viscosity ν_a and the windsea spectrum peak angular frequency ω_p, thus describing turblence at the wind-wave boundary. The role of wave breaking mechanisms on generation has also been a focus of study with the use of whitecap coverage to scale film, jet (Laussac et al., 2018) and spume droplet generation (Anguelova et al., 1999). In a similar fashion, wave energy dissipation - considered proportional to u_*^3 (the third power of the friction velocity u_*) by several authors - has also been considered for the study of

droplet and bubble generation (Newell and Zakharov, 1992; Zhao and Toba, 2001; Zhao et al., 2006; Andreas, 1998, 2002; Fairall et al., 2009).

Of the different wave parameters used to scale sea spray generation, the wave slope has not yet been considered. Nevertheless, it is an interesting candidate because of its strong relation to wave breaking (Stokes, 1880; Duncan, 1981; Ramberg and Griffin, 1987), whitecap production (Banner et al., 2002; Brumer et al., 2017), and therefore to sea spray bubble-bursting and surface-tearing generation mechanisms. The wave slope, however, is also thought to modulate the air flow at the wave crest (Veron, 2015; Richter et al., 2019; Husain et al., 2019), which is of crucial importance for air-sea momentum transfer and surface tearing mechanisms. Finally, the relationship between the wave slope variance and the wind speed at the wind-wave boundary is relatively well documented (Cox and Munk, 1956; Plant, 1982; Vandemark et al., 2004; Bringer et al., 2013; Lenain et al., 2019).

With the advantage of easier instrumentation and control over important environmental parameters compared to the complexity of the field, the laboratory has proven to be a valuable alternative to the field (open ocean) for the study of wave-wind boundary processes and sea spray generation (Toba and Koga, 1986; Fairall et al., 2009; Ortiz-Suslow et al., 2016; Troitskaya et al., 2018). Therefore, we conducted a series of experiments in the wave-wind tunnel at the OSU Pytheas (Observatoire Sciences de L'Univers) Ocean-Atmosphere laboratory in Luminy, France. In the field, a wide range of wind and wave combinations can be encountered. To reproduce a similar range in environmental conditions the laboratory experiments also included a unique range of wind and wave conditions, which, to the knowledge of the authors, is the most extensive range ever used for studying the SSGF in a laboratory configuration. The aim is to develop a universal wind and sea state-dependent SSGF

applicable for radii typical of jet and spume droplets. To this end, from June to July 2019, sea spray aerosol size concentrations were measured for a total of twenty wind and wave combinations as part of the Marine Aerosol Tunnel Experiment (MATE2019). The experiment is described in Sect. 2, wind and wave results are discussed in Sect. 3, and sea spray results in Sect. 4. Study results include a comparison between the laboratory data and other laboratory and field SSGFs presented in the literature. Finally, two new SSGFs are introduced in Sect. 5, one depending on the wave slope variance alone, and a second on both the wave slope variance and u_*^3. Both SSGFs combine laboratory and field data, and are valid for wind speeds 12-20 m s^{-1} and radii 3-35 μm.

2 Methods

2.1 The wind-wave tunnel

The UMS Pytheas ocean-atmosphere interactions facility at Luminy (Marseille, France), schematically represented in Fig. 1, consists of a water tank with a wind tunnel on top of it. The facility currently allows the use of fresh water only. The water tank is 40 meters long, 2.6 meters wide, and has a wave-dissipating beach at the downwinde end to avoid wave reflection. On the upwind end, the facility is equipped with a programable submerged piston-like wavemaker located at the bottom of a cavity below the air tunnel and controlled by an electrohydraulic motor. Wave properties such as amplitude, frequency and slope can therefore be selected. Waves can attain amplitudes reaching 15 cm, approximately. The air channel ceiling is slightly inclined to the fetch to avoid the airflow acceleration and the related longitudinal pressure

gradient generated by the thickening of the wall and water surface boundary layers (Coantic et al., 1981). To reduce turbulence as the air flow encounters the water surface, a thin buoyant sheet is placed at the surface of the water at the entrance of the tunnel. The wind speed in the facility is adjustable, with winds reaching 15 m s^{-1}, approximately. Glass walls on either side of the laboratory made it possible to monitor the experiment at the location of the instruments (given below).

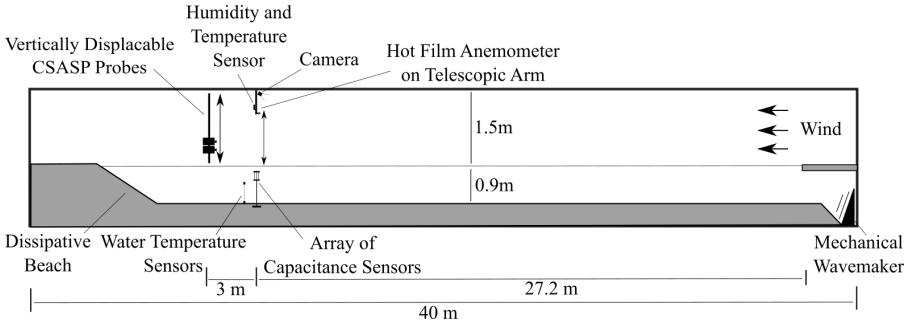

Fig. 1 Side view of the experimental configuration in the laboratory

For the experiments in June-July 2019, the water depth was set to 90 cm, leaving 150 cm between the water surface and the ceiling of the wind tunnel. As schematically represented in Fig. 1, instruments used for the measurements of air, water, wind and wave characteristics were placed at the 27.2 meter fetch mark. A sensor positioned 81 cm above the mean water level (MWL) was used to measure air relative humidity (RH) and temperature (T_a). Vertical profiles of horizontal wind speed and air temperature between 15 and 66 cm above MWL were obtained using sensors mounted on a telescopic arm. The water temperature was measured at both 20 and 60 cm depth beneath the MWL. A camera with 60 Hz sampling frequency placed on the tunnel ceiling allowed estimating the whitecap coverage during the experiments from color images. Though not schematically represented in Fig. 1 a higher-frequency 128 Hz camera was used to film through the glass wall of the tunnel for monitoring purposes only. Finally, at the 30 meter fetch mark, vertical profiles of the sea

spray number concentration were measured using two particle probes mounted onto a vertically displaceable frame.

2.2 Wave generation and characterisation

The water surface elevation was measured by an array of two calibrated capacitance wave gauges placed at the 27.2 meter fetch mark. The sample frequency for the wave gauges was 256 Hz allowing to sample a wide range of wave surface elevation and slope frequency spectra. The sensors were aligned orthogonally to the general wave direction, and were placed 1 cm from each other to ensure accurate wave slope measurements.

In the present study, four types of waves were generated. Five different wind speeds between 8-20 m s^{-1} were applied over each wave type, in a total of 20 laboratory wind-wave configurations. A first type of waves was generated solely by the wind, resulting in pure wind waves. The other three types of waves were generated using the piston wavemaker and are referred to as short wave forcing (peak frequency $f_p = 1.3$ Hz and wavelength $\lambda = 0.92$ m), intermediate wave forcing ($f_p = 1.1$ Hz and $\lambda = 1.29$ m), and long wave forcing ($f_p = 0.8$ Hz and $\lambda = 2.4$ m). These conditions were selected to ensure that near-equilibrium with the overlying wind field was either never met, or met at different wind speeds. Deep water conditions are theoretically confirmed for all types of forcing except the long wave case. This is also the wave type that is least forced by the wind and can be considered representative of the wind over swell condition that can be found in the field. Together, the 20 tunnel wind and wave combinations span a range of wave ages $\frac{c_p}{u_*}$ between 1.3 and 9.6.

The wave sensor array provides several parameters that are useful to relate the wave properties measured at the 27.2 m fetch mark to the sea spray concentrations measured at the 30 m fetch mark. The significant wave height H_S is determined using:

$$H_s = 4\sigma_\eta$$

where σ_η is the standard deviation of the surface elevation (η) time series measured by the wave sensor array.

The wave slope variance $< S^2 >$ is considered equal to the wave mean square slope (MSS). It is calculated from the time series of the wave slope S, for wavelengths $\lambda > 1$ cm (strong majority of waves dominated by gravity). The use of classical Fourier analysis allows to determine the peak frequency f_p from the wave elevation energy spectra. Finally, the wave phase speed c_p is determined from the phase shift between the wave gauges as the waves propagated along the wave sensor array.

2.3 Whitecap measurements

To quantify the wave breaking, the whitecap coverage *W(%)* is estimated from video colour images taken by a camera mounted at the tunnel ceiling (cf. Fig. 1). The system takes images at 60 Hz frequency with dimensions 2704 × 2028. These images are spatially referenced to allow to estimate the approximate surface area of each pixel. To identify the whitecaps, a separation method is used that applies a greyscale conversion and a subsequent intensity threshold to the image. The surface areas of the pixels above threshold are subsequently added and divided by the total image surface area for an estimate of the

whitecap surface coverage *W(%)*. Using a time series of images, it was found that *W(%)* estimates converge to an average value within approximately 120 frames. This method for whitecap estimation is commonly used (e.g. Lafon et al. (2007); Lenain and Melville (2017); Brumer et al. (2017)), and although the selection of the intensity threshold may be subjective, we expect that our whitecap coverage estimates capture the relative amount of wave breaking induced by various wind and wave conditions.

2.4 Wind measurements

A hot film wind sensor (E+E Elektronik, Langwiesen, Austria) mounted onto a telescopic arm was used to measure vertical profiles of horizontal wind speed U at the 27.2 meter fetch mark (cf. Fig. 1). This sensor was calibrated against a reference sonic anemometer on several occasions during the experiments. Some subsets of wind data obtained at 15 cm of the MWL were eliminated from the dataset to avoid erroneous measurements caused by large droplets impacts on the hot film sensor. To ensure representative wind statistics, convergence of the wind speed time-averages was achieved for each height z along the *U(z)* profiles, with averages spanning over 20 to 80 minutes in accordance with the sea spray aerosol sample durations.

The wind speed reference used in this study is U_{10}, i.e. the wind speed at 10 meters above MWL. Assuming a logarithmic wind profile and neutral conditions, Monin and Obukhov (1954) scaling allows evaluation of U_{10} (m s^{-1}) and the friction velocity u_* (m s^{-1}) from the measured $U(z)$ profile values *U(z)*:

$$U(z) = \frac{u_*}{k} ln(\frac{z}{z_0}) \tag{1}$$

where $k = 0.4$ the von Kármán constant, z is the measurement height above MWL, and z_0 the roughness length. The latter is retrieved by extending the wind profile with data from the more elevated part of the wind profile that is not significantly affected by the wave field. During the experiments, z_0 estimates varied between 0.2 and 2.5 mm.

Figure 2 presents the experimental wind profiles for all 20 laboratory configurations (data points with horizontal error bars) as well as the corresponding theoretical profiles obtained with Eq. 1. For clarity and indicative purposes only, are also presented the average friction velocities $< u_* >$ calculated over the 4 different wave types for each individual tested wind speed. The experimental profiles exhibit near-logarithmic behaviour, and the gradient increases for increasing reference wind speed U_{10}, in accordance with a fully developed turbulent layer near the water surface as encountered in the field. This is further evidenced by the windsea Reynolds number (R_B) found greater than 10^3 in the laboratory for reference wind speeds U_{10} of 12 m s^{-1} or more, thereby signifying that the air flow in the boundary layer is in a fully turbulent regime and windsea breaking occurs (Toba et al., 2006).

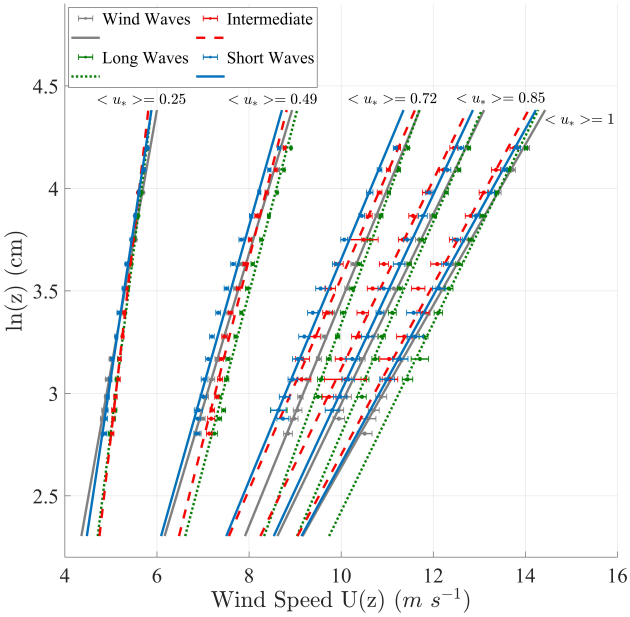

Fig. 2 Measured *U(z)* profiles for all twenty laboratory configurations (horizontal bars) with associated theoretical profiles (lines) calculated with Eq. 1. Average friction velocities values $< u_* >$ pertain to the five wind speeds set in the laboratory.

2.5 Sea spray aerosol measurements

The measurement of sea spray in the tunnel was carried out using two CSASP (Classical Scattering Aerosol Spectrometer) probes (Particle Measurement Systems, Boulder, Colorado, USA). This type of probes has been proven reliable in numerous experiments by the authors and others (e.g., Frick and Hoppel (2000); Savelyev et al. (2014); Petelski et al. (2014)). Our two probes have overlapping particle radius ranges allowing a combined range of 0.1 to 47.5 μm. Prior to the experiments, both probes were calibrated with latex particles of known sizes. The CSASP-100-HV-ER probe samples by rotating over 4 sets of 15 size bins at a time, in total spanning from 0.5 to 47.5 μm radius. The CSASP-200, samples over a single set of 31 size bins ranging from

0.1 to 10 μm radius. The probes send data to the controller every second, and aerosol number concentrations for each bin size are obtained by averaging over a chosen sample (integration) time. Since number concentrations were expected to decrease with increasing height above the water surface, sample times varied from a minimum of 20 minutes at $z = 35$ cm to a maximum of 80 minutes at $z = 82$ cm in order to improve droplet count statistics. Nevertheless, particle concentrations for radii greater than 35 μm were statistically unreliable and had to be discarded. It was verified that droplet concentrations were stationary over the duration of the experiment once equilibrium for a particular laboratory configuration was established.

During the experiments, the probes were placed on top of each other. Droplet number concentrations were measured at five different heights for each of the twenty laboratory configurations. For the CSASP-100-HV-ER, samples were made at heights $z = 35$, 41, 51, 65 and 82 cm above the MWL. These heights are used as reference in this study, and the CSASP-200 concentrations are interpolated to these heights. The air flow inside a long wind-tunnel is not completely homogenous, and very slight transverse counter-rotating streamwise vortices or cells may appear (Holmes et al., 1996; Pope, 2000), with a very weak divergence or convergence zone along the middle of the width of the tunnel. As it is usually done in the IRPHE wind-wave facility, the probes were slightly shifted away from the middle axe line of the facility. For all laboratory configurations, both aerosol probes were temporarily positioned at the tunnel entrance to verify that no background aerosols entered the tunnel, which implies that all particles detected at the 30 m fetch mark are solely produced over the upwind 30 meter fetch length.

After generation at the water surface, the hygroscopic aerosols adjust their size to the ambient humidity and temperature of the air flow. This process is

different for salt water than for the fresh water used in the tunnel, as freshwater droplets can evaporate more quickly and completely than saltwater droplets that reach an equilibrium size (e.g. Pruppacher and Klett (1978); Andreas (1989); Fairall (1990); van Eijk et al. (2001); Mueller and Veron (2014); Mehta et al. (2019)). During the experiments, the relative humidity (RH) in the laboratory varied between 79 and 82%, with an average water temperature at 0.2 m depth of 18°C, and an average air temperature T_a at 85 cm height of 25°C. We therefore assume that sea spray number concentrations correspond (roughly) to $RH = 80\%$. Since the rate of freshwater droplet evaporation at $RH = 80\%$ is relatively small, we assume that out measured droplets are representative for saltwater droplets at their $RH = 80\%$ equilibrium radii. However, this assuption will fail if the freshwater droplets are relatively small or have long residence times before reaching the aerosol probes, as evaporation can become substantial (Veron, 2015). To avoid such evaporation effects over the length of the wave-wind facility, only radii greater than 7 μm are considered for the source functions proposed in this study (see Sect. 5) in accordance with Fairall et al. (2009).

Aerosol concentrations are often expressed as number concentrations dN/dr (cm^{-3} $\mu\mathrm{m}^{-1}$; the number of particles N of a given radius r measured per unit air) or volume concentrations dV/dr (the volume for a given radius measured per unit air). In this study, we use mostly number concentrations, with a single exception (Sect. 4, Fig. 6). The conversion from number to volume concentrations (cm^{-3} cm^{-3} $\mu\mathrm{m}^{-1}$) is made by assuming that the droplets are spherical:

$$\frac{dV}{dr} = \frac{dN}{dr}\frac{4}{3}\pi r^3 \tag{2}$$

As discussed above, we may consider that the freshwater droplet distributions measured in the tunnel are analogous to salt water droplets at $RH = 80\%$.

Since the processes that generate the freshwater droplets in the tunnel are the same as for sea spray in the field, we will denote the droplets in the tunnel as sea spray in the remainder of this paper.

3 Tunnel wave and wind results

3.1 Wave measurements

Table 1 characterises all 20 laboratory configurations in terms of the significant wave height H_s, the wave slope variance $< S^2 >$, the friction velocity u_*, and the whitecap coverage *W(%)*. The table shows that the wind field forces the wave field, resulting in increased wave height, wave slope variance and breaking, as evidenced by H_s, $< S^2 >$ and *W(%)*. In some cases however, significant wave height and wave slope decrease for high wind speeds as wave energy dissipation by wind-induced breaking becomes temporarily greater than the energy input from the wind to the waves. This is especially the case for the intermediate wave forcings for wind speeds increasing from 16 to 18 m s^{-1} (Table 1) where wave breaking was especially high. Further evidence of the forcing of the wave field by the wind is the decrease in f_p for increasing wind speed observed at the 27.2 fetch mark, with the exception of the long wave forcing which conserves the 0.8 Hz frequency prescribed by the wavemaker throughout the experiments. The momentum transfer from the wind to the waves is therefore relatively low for the long wave forcing in comparison to the other wave forcings, resulting in relatively low *U(z)* gradients (Fig. 2) and whitecap coverages *W(%)* (Table 1).

Table 1 Wave-wind boundary characteristics for the different laboratory configurations: significant wave height H_s (cm), wave slope variance ($< S^2 >$), friction velocity u_* (m s^{-1}), wave phase speed c_p (m s^{-1}) and whitecap coverage $W(\%)$

Forcing	H_s	$< S^2 >$	u_*	c_p	W(%)	H_s	$< S^2 >$	u_*	c_p	W(%)
	U_{10} = 8 m s^{-1}					U_{10} = 12 m s^{-1}				
Wind	3.2	0.026	0.32	0.78	0.13	5.5	0.039	0.54	0.99	0.29
Short	9.7	0.037	0.28	1.19	0.28	12.4	0.053	0.52	1.29	0.62
Inter.	13.2	0.033	0.21	1.42	0.32	16.7	0.047	0.46	1.49	0.53
Long	12.0	0.024	0.23	2.2	0.16	13.8	0.03	0.48	1.7	0.25
	U_{10} = 16 m s^{-1}					U_{10} = 18 m s^{-1}				
Wind	8.3	0.056	0.75	1.1	0.8	9.63	0.062	0.89	1.25	1.25
Short	13.7	0.063	0.76	1.33	1.17	15.4	0.066	0.85	1.54	1.45
Inter.	20.1	0.087	0.8	1.50	2.55	18.4	0.08	0.89	1.59	4.65
Long	16.5	0.046	0.66	2.1	0.73	19.6	0.055	0.79	2.14	0.84
	U_{10} = 20 m s^{-1}									
Wind	11.3	0.073	1.05	1.32	2.0					
Short	15.2	0.072	1.01	1.63	2.25					
Inter.	17.6	0.078	1.0	1.57	3.19					
Long	21.6	0.065	0.9	2.15	1.19					

This non-linear behaviour of the parameters listed in Table 1 highlights the importance of correctly understanding the boundary processes, such as the state of wind-wave equilibrium. Though not shown here, f^{-5} and f^{-4} spectral shapes were identified for the individual wave spectra, but it proved difficult to quantify the wave-wind equilibrium this way. We therefore abide by the heuristic idea that when the phase speed c_p is greater than the overlying wind speed (e.g. the friction velocity u_*) then the underlying waves are no longer forced by the wind field. Thus we use the wave age defined as c_p/u_* to quantify the wind-wave equilibrium.

Our laboratory configurations yield wave age c_p/u_* values ranging from 1.3 to 9.6 where the higher values correspond to the long wave forcing combined with the lowest wind speed (8 m s^{-1}). These values are generally lower than those recorded in the field because of the comparatively much shorter fetch length in the laboratory.

3.2 Whitecap measurements

As previously noted, several studies have related whitecapping to the generation of film, jet and spume droplets. For comparison, it is therefore important to ascertain whether the whitecap production in the laboratory differs from the field. To this end, we use data collected during the EMMA campaign which took place in Toulon-Hyeres bay, yielding wave, wind and whitecap coverage data for wind speeds in the 10 - 18 m s^{-1} range and wave ages c_p/u_* in the 14 - 28 range Lafon et al. (2007). We compare our laboratory whitecap coverage to that measured in fetch-limited field conditions during EMMA, using a similar image-processing technique with intensity threshold separation (data available in Lafon et al. (2007)). Laboratory data obtained at 8 m s^{-1} wind speed are not included in this comparison because the relatively small amount of wave breaking may reduce the accuracy of the whitecap coverage estimates.

Multiple independent scaling studies have proven R_B to be a successful scaling tool for *W(%)* (Zhao and Toba, 2001). However, the evaluation of R_B requires the wave peak frequency ω_p, which differs significantly between the laboratory and the field. The relatively short fetch in the laboratory and the wavemaker settings lead to shorter wavelengths and a relatively greater number of wave crests per unit area (Mueller and Veron, 2009). To allow a better comparison between the laboratory and the field, the *W(%)* value are therefore normalised by the wave peak frequency. Figure 3a shows the relationship between the normalised *W(%)* and R_B. The data from both the laboratory (+) and the field (▼) display a very similar trend yielding nearly identical slopes when fitted by a power law. In absolute magnitude there is a factor 1.5 difference between the laboratory and the field with the lower *W(%)* values for the laboratory. A possible explanation is the absence of surfactants

and salt in the laboratory, which in the field contribute to whitecap formation and increase whitecap lifetime (Callaghan et al., 2012). Consequently, the lower rate of whitecap formation and lifetime in the laboratory may signify that our whitecap coverage is more representative for the process of active wave breaking, which we refer to as the wave breaking coverage.

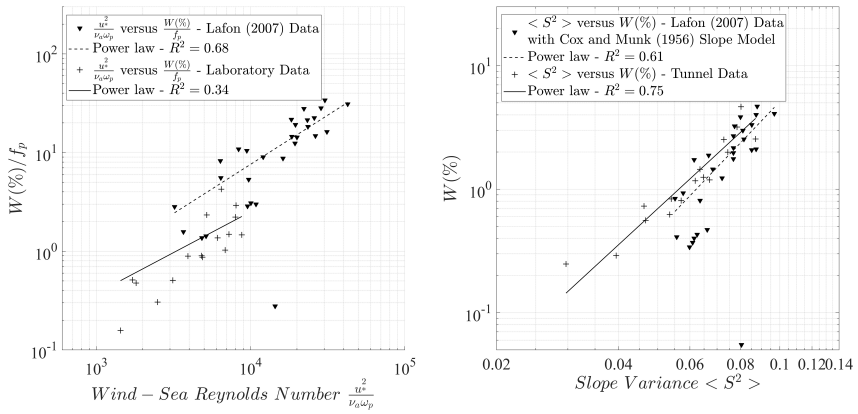

Fig. 3 Comparison between laboratory and field (Lafon et al., 2007) (a) f_p-normalised whitecap coverage *W(%)* estimates as function of the windsea Reynolds number R_B, and (b) *W(%)* as function of the wave slope variance $< S^2 >$. Lines and corresponding R^2 statistics represent power laws fitted to the data.

A further comparison between the laboratory and the field is obtained by scaling *W(%)* to the wave slope variance $< S^2 >$. In this case, *W(%)* does not need to be normalised by the peak frequency as the wave slope variance $< S^2 >$ integrates a very large part of the wave frequency spectrum and corresponding wave slopes, unlike the peak wave characteristics required for windsea Reynolds number R_B. For the EMMA campaign data (Lafon et al., 2007), $< S^2 >$ is estimated from the measured wind speed data (Cox and Munk, 1956) :

$$< S^2 >= 0.003 + 5.12 \times 10^{-3} U_{12.5} \pm 0.004 \tag{3}$$

where the wind speed $U_{12.5}$ is calculated from the EMMA campaign U_{10} measurements using classical Monin and Obukhov (1954) theory. It is worth noting that Eq. 3 (Cox and Munk, 1956) was determined from airborne observations of sun glitter resulting in the contribution of a wide range of wave scales including non-breaking waves, which is to some extent comparable to the wide range of wavelengths included in the laboratory wave slope variance.

Figure 3b presents the $W(\%)$ scaling by $< S^2 >$, demonstrating that laboratory (+) and field (▼) data almost overlap. The laboratory data is well fitted ($R^2 = 0.75$) by a the power law:

$$W(\%) = 6.02 \times 10^3 < S^2 >^{3.025} \tag{4}$$

The good fit of this power law to field data (Fig. 3b) suggests that Eq. 4 may have a validity range extending to both the laboratory and the field. The strong correlation between $< S^2 >$ and $W(\%)$ suggests that the wide range of the wave slope spectrum inherent to $< S^2 >$ allows to separate breakers and non breakers. This corroborates conclusions from a north-Pacific field campaign (Schwendeman and Thomson, 2015), where the wave slope variance amongst the different existing slope parameterizations is found to scale best with $W(\%)$ by considering the slopes of the shorter waves, thought to be important for whitecap production. In contrast, the scaling of whitecap coverage with wave steepness (often written as $H/(2\lambda)$) has proven difficult (Schwendeman and Thomson, 2015) or even unsuccessful (Holthuijsen and Herbers, 1986).

4 Laboratory sea spray results

4.1 Sea spray aerosol size distribution spectra

Figure 4 presents two typical size distributions as measured in the laboratory. The figure shows the sea spray distributions for wind speeds $U_{10} = 16$ m s^{-1} and $U_{10} = 20$ m s^{-1}, measured 55 cm above MWL and during the intermediate wave forcing. For convenience, polynomial functions (solid and dashed lines for 16 and 20 m s^{-1}, respectively) have been fitted to the distributions. The polynomial functions show that the number concentration of all but the smallest particles increases with increasing wind speed. This behaviour is observable at any height above MWL and for all four types of wave forcing. The concentration increase is consistent with the increased *W(%)* for increasing wind speeds (cf. Table 1) and hence, the enhanced droplet generation. Furthermore, the size distribution shows a relative abundance of particles with sizes around 1 and 10 μm. This corroborates the established size ranges of film and jet droplets, respectively. The droplet spectra for larger radii change markedly at wind speeds lower than 12 m s^{-1}, where number concentrations for $r > 15$ μm are negligible. This corroborates the assumption that these larger droplets are predominantly spume droplets, and that their generation mechanism activates at wind speeds around 12 m s^{-1}. This was confirmed by our high-speed video footage, which revealed surface tearing and bag break-up only for wind speeds higher than 12 m s^{-1}. In conclusion, the above observations suggest that similar droplet generation mechansisms are active in the laboratory and in the field.

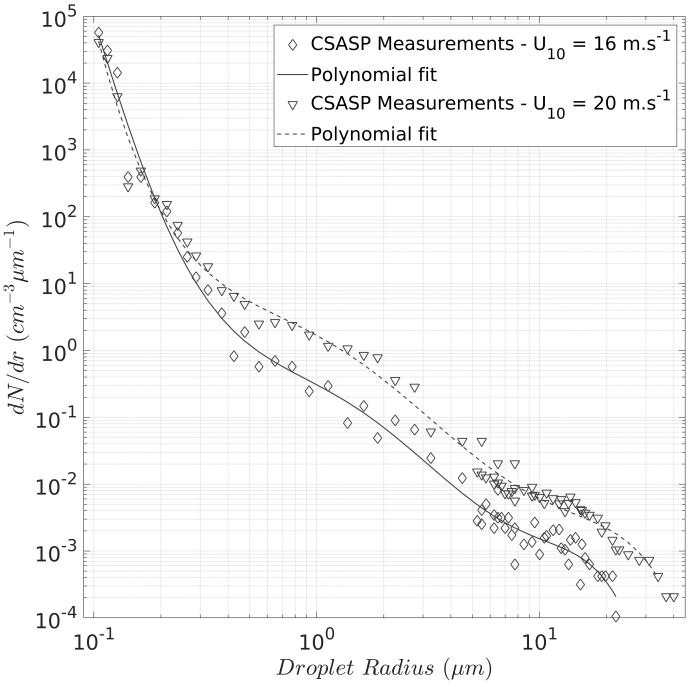

Fig. 4 Sea spray number concentration size distribution at 55 cm above the MWL for the intermediate wave forcing.

Let us now consider the vertical distribution of the freshly generated particles. Figure 5 shows number concentration profiles obtained at $U_{10} = 20$ m s^{-1} as a linear function of the natural logarithm of height $ln(z)$. Two sets of profiles are shown, for droplets of 10 and 20 μm radius, and each set contains data for the four different types of wave forcing. The symbols of individual data points refer to the type of wave forcing. The lines denote linear functions fitted on the experimental data. Figure 5 suggests that the vertical number concentration profiles of sea spray are near-logarithmic with height above MWL. This behaviour is general for all radii in the 7-35 μm range. For the three highest wind speeds, R^2 values of the individual fits all exceed 0.95. Though not presented in Fig. 5 for clarity, the standard deviation in number concentrations is

highest closest to the water surface, especially for intermediate and short wave forcing, but remains very small with a maximum value approaching 10^{-5} cm^{-3} μm^{-1} at $z = 0.35$ m. As the environmental conditions were stationary during the measurements for each individual laboratory configuration, this greater variability (standard deviation) in near-surface concentrations could be associated with wave-induced and phase-locked modulation of the airflow, which can lead to flow separation. These mechanisms have recently been observed in microphysical laboratory experiments (Buckley and Veron, 2019; Richter et al., 2019; Husain et al., 2019). Whether this modulation effect also caused stronger fluctuations in the near-surface sea spray concentrations in the laboratory remains hypothetical as the maximum sample frequency of the particle probes does not allow to resolve these fluctuations assumed to occur at frequencies approaching f_p or higher.

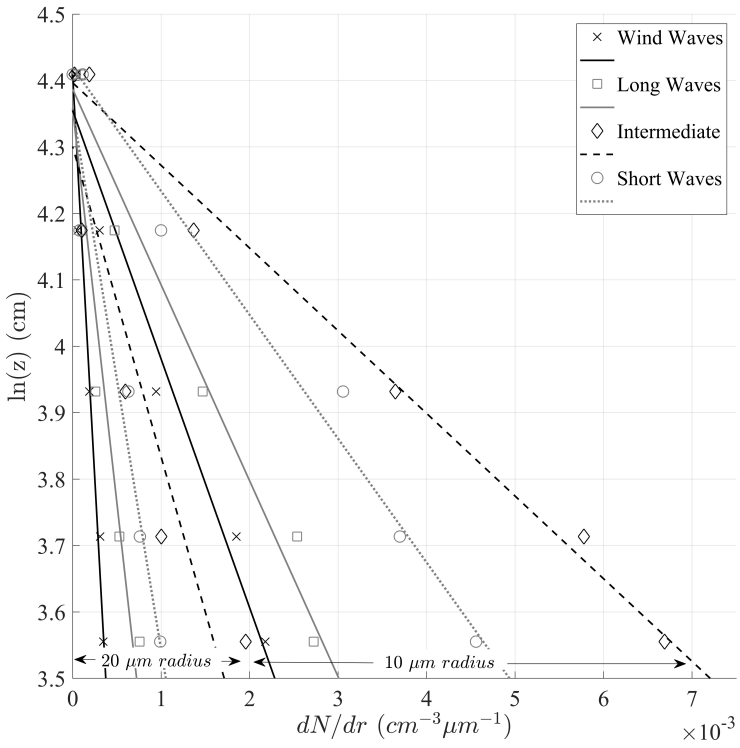

Fig. 5 Sea spray number concentration profiles at 20 m s^{-1} winds as function of height, represented as *ln(z)*. Symbols denote experimental data, lines linear fits to the data.

Figure 5 also demonstrates that the type of forcing affects the vertical concentration gradients. The stronger gradients are observed for intermediate and short wave forcings, whereas the forcing by wind alone results in a less pronounced concentration decrease with height. To further investigate the effect of sea state, Fig. 6 focuses on the aerosol size distributions over the 6 - 47.5 μm radius range obtained at $z = 35$ cm, and for wind speed $U_{10} = 20$ m s^{-1}. Individual datapoints represent an average over several particle bin sizes (spanning $\pm$ 4 μm) for clarity, and horizontal and vertical error bars illustrate the standard deviations in average size and concentration, respectively. The data is presented on a log-log scale, and individual datapoints are connected

by lines to provide an indication of the volume spectrum. As identified by the legend in Fig. 6, we present data for the four types of wave forcings using in the laboratory.

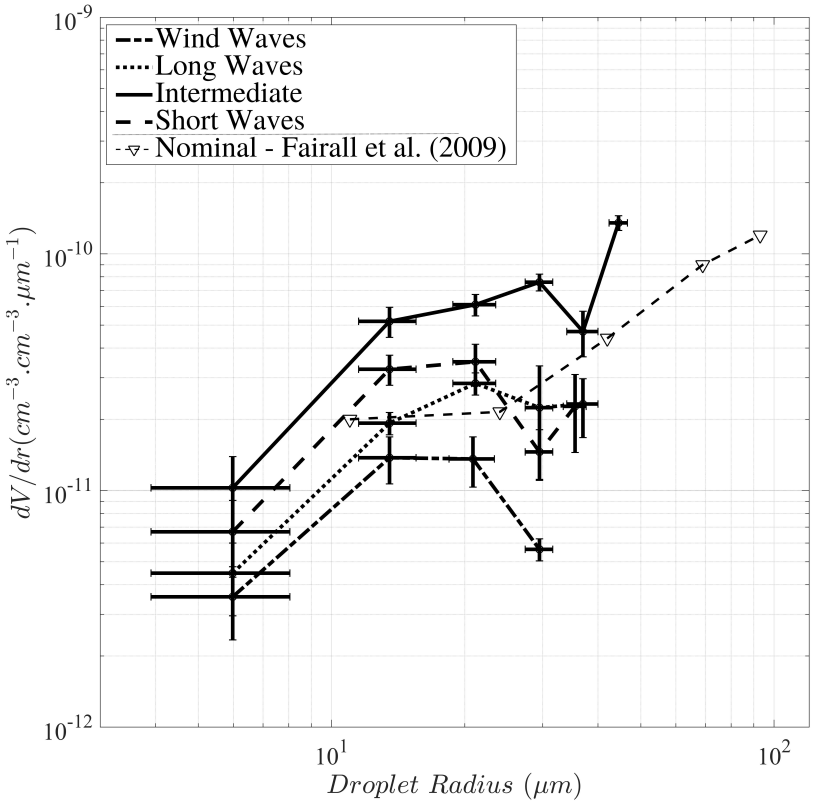

Fig. 6 Sea spray volume concentrations for $U_{10} = 20$ m s^{-1} at 35 cm above the mean water level, for the four forcings used in the laboratory. SPANDEX data measured at 31.5 cm above MWL corresponding to their nominal condition is presented for comparison.

Figure 6 depicts volume rather than number concentrations. Comparing with Fig. 4 reveals that while large droplets are less numerous, they represent the larger part of the volume (or mass). Presenting the data as volume concentrations allows us to better detail the differences between the four types of wave forcing. Visual comparison of the four curves reveals that wind forcing alone results in the lowest concentrations (dashed curve) and a distribution that strongly decreases for $r > 20$ μm. The three wavemaker forcings all re-

sult in higher volume concentrations than the wind forcing: the order long, short and intermediate for increasing concentration corresponds well with the increase in whitecap $W(\%)$ and wave slope variance $< S^2 >$ for these three types of forcing (cf. Table 1), and hence, the production of droplets.

A literature survey for comparison laboratory data identified the SPANDEX dataset (Fairall et al., 2009) as the most suitable. These authors also used a wind-wave interaction tunnel with freshwater and a mechanical wave paddle for the wave forcings. The triangles in Figure 6 (connected by the thin dashed line) represent the volume concentrations reported by Fairall et al. (2009), obtained at 31.5 cm height for 16.7 m s^{-1} wind speed (corresponding to their nominal forcing) measured at 40 cm above MWL (roughly equivalent to 28 m s^{-1} at U_{10}), 1.36 Hz peak wave frequency (same as our short wave forcing), and friction velocity $u_* = 1.44$ m s^{-1}. Though the wind speed and friction velocity were 50 % greater than for the present study, the SPANDEX volume concentrations are of the same order of magnitude as our wave-forced data (cf. Fig. 6). This unexpected overlap may be explained by experimental differences such as tunnel dimensions (more than three times the height between the water surface and the tunnel ceiling during MATE2019 compared with SPANDEX) leading to possibly different boundary effects. Another explanation maybe also be related to the different wave amplitudes between both experiments ($\approx$ 5 times greater in the present study) resulting in shorter distances between the probes and the wave crests in the case of MATE2019 despite comparable sample heights in the present comparison.

4.2 Scaling parameters for the sea surface sea spray generation

In the previous section we have demonstrated that the sea spray concentration depends on properties of both the air flow and the sea state. To bridge these two domains, we will scale the sea spray surface generation using non-dimensional numbers representing the physical processes on the wind and wave side of the wave-wind boundary. The non-dimensional numbers determined from the set of parameters (u_*, ω_p, c_p, H, λ, X, g, ρ_a, ρ_w, ν_a, ν_w, Γ), where u_* is the friction velocity, ω_p is the wave peak angular frequency, c_p is the wave phase speed, H is the wave height, λ is the wavelength, X is the fetch length, g is gravitational acceleration, ρ_a and ρ_w are air and water densities respectively. Furthermore, ν_a and ν_w are air and water kinematic viscosities, respectively, and Γ is the water surface tension.

As a first step, we focus our attention on the air kinematic viscosity. Several studies have indicated that water droplets and water vapor can alter the air viscosity, but the effect on the momentum flux is thought to be small, less than 3% (Fairall et al., 2009). We therefore consider the non-dimensional groups ν_a/ν_w and ρ_a/ρ_w to be constants. We also expect the surface tension Γ to be constant and remain negligible due to the relatively long wavelengths considered here (strong majority of gravity waves). Then, we can express the sea spray aerosol generation flux as a function of the non-dimensional numbers that are the inverse wave age ($= u_*/c_p$), the windsea Reynolds number R_B ($= u_*^2/(\nu_a\omega_p)$, determined from both wind (u_*) and peak wave (ω_p) characteristics), and the wave steepness. In continuity with the previous sections, the wave slope variance $< S^2 >$ is used instead of the wave steepness ($H/2\lambda$). The inverse wave age is preferred to the wave age out of physical coherence, as the former is expected to increase for increasing R_B and $< S^2 >$. We create

a fourth scaling parameter by combining the inverse wave age, the windsea Reynolds number and the wave slope variance:

$$P_S = R_B < S^2 > \frac{c_p}{u_*}^{-1}$$

which, considering the deep water dispersion relation $c_p = \frac{g}{2\pi}T$ (T the wave period), reduces to:

$$P_S = \frac{u_*^3}{\nu_a g} < S^2 > \quad (5)$$

where P_S, adding to the P threshold for the activation of droplet and bubble formation at the water surface (Newell and Zakharov, 1992; Fairall et al., 2009), describes the wave slope variance-modulated wind energy input to the waves. This number combines two experimental quantities, $< S^2 >$ provided by the wave sensor array, and u_*^3 provided by the wind speed vertical profiles, providing information on the wind-dependent sea state and wind-induced dissipation, respectively. This allows to study air-sea interaction processes from a multiscale point of view, assuming that the smaller and larger scale wind and wave components significantly contribute to boundary layer mechanisms responsible for sea spray generation.

4.3 Scaling of the sea spray generation

This section discusses the scaling of the sea spray by the four scaling parameters introduced above. For this, we use the concentrations measured 35 cm above the MWL, i.e., the lowest height of our aerosol samplers, assumed the most representative of the generation flux and the least affected by size-dependent vertical dispersion effects similar to Wu (1993) and Andreas (1998). The scaling relationships are presented for droplet radii of 7.5 μm (Fig. 7) and

548 25 μm (Fig. 8), which are considered representative of the behaviour of the
549 droplets in the 7-20 μm and the 20-35 μm size range, respectively. In this man-
550 ner, we provide separate scaling for the sea spray predominantly produced by
551 bubble bursting (7-20 μm) and surface-tearing (20-35 μm) mechanisms.

552 Figures 7a and 8a report the scaling with wave age. The presented data
553 correspond to the wind-wave (blue dots), long wave (pink dots), intermediate
554 wave (red dots) and short wave (green dots) forcing at 16, 18 and 20 m s^{-1} U_{10}
555 wind speeds. Data of the same type of forcing are fitted to a linear function,
556 denoted by a dashed line of the same colour. The black solid line represents a
557 linear fit to all 12 datapoints, and the R^2 value of the fit is given in the graphs
558 ($R^2 = 0.13$ for scaling with wave age for particles of 7.5 μm). Although the
559 wave age seems to correctly scale concentrations for individual wave forcings,
560 no clear relationship is found between the measured concentrations and wave
561 age when all data is included. Therefore, we conclude that wave age is not
562 well suited for the scaling of sea spray generation for both young wind-forced
563 waves, and older swell-type waves.

564 Nevertheless, it is interesting to further discuss Figs. 7a and 8a. The overall
565 decrease in near-surface concentrations for increasing wave age (Figs. 7a and
566 8a) corroborates observations made in the field, as less whitecap is produced
567 by older swell-type waves or wind waves modulated by older waves in contrast
568 with wind waves alone (Schwendeman and Thomson, 2015; Brumer et al.,
569 2017). Both figures show that relatively high sea spray concentrations are
570 found for the intermediate and short forcings, with corresponding wave age
571 values of approximately 1.7. This can be expected considering the high values
572 of $W(\%)$ and $< S^2 >$ for these types of forcing (cf. Table 1). High droplet
573 concentrations associated with young, steep and strongly breaking waves is
574 typical of fetch-limited wave fields (Lafon et al., 2007). Specifically, for the

larger 25 μm particles (cf. Fig. 8a) such a peak can be related to droplet ejection microphysics as younger steeper waves induce airflow separation (Reul et al., 2008), thought to play an important role in droplet ejection from the wave crests (Mueller and Veron, 2009; Veron et al., 2012; Richter et al., 2019).

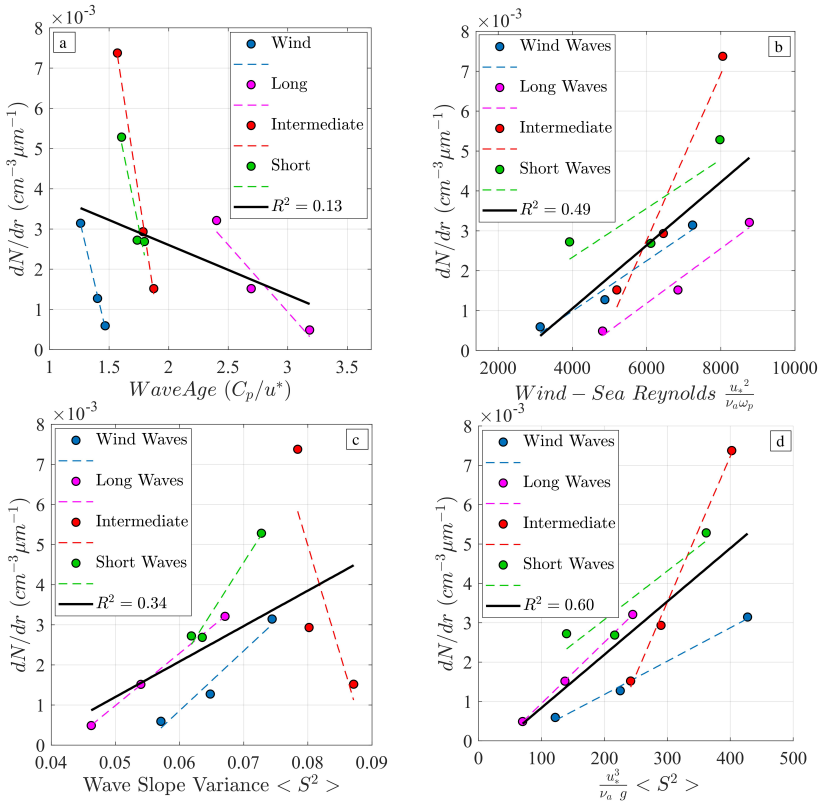

Fig. 7 Scaling of dN/dr with (a) wave age, (b) R_B, (c) $< S^2 >$ and (d) $P_S = \frac{u_*^3}{\nu_a g}.< S^2 >$ for particles of radius 7.5 μm, 35 cm above MWL. Individual types of wave forcing are represented in color, with U_{10} wind speeds ranging from 16 to 20 m s^{-1}. Solid black lines in all panels represent linear fits to all 12 datapoints.

We now turn our attention to Figs. 7b and 8b, which present the windsea Reynolds number R_B as a scaling parameter for the sea spray concentration. The Reynolds number has proven to be strongly related to whitecap coverage and wave breaking (cf. Sect. 3.2) as well as sea spray concentrations for wind waves especially (Iida et al., 1992; Toba et al., 2006; Troitskaya et al., 2018). This seems confirmed by the overall (solid black line) trend line in Figures

7b and 8b, which is relatively close to the data corresponding to wind waves. The data show less spread than for scaling with wave age, and most types of forcing follow the overall trend, despite systematic differences in droplet concentrations. The overall fit quality for the 7.5 μm particles amounts to R^2 = 0.49 and similar values were noted for other radii in the 7-20 μm range. The windsea Reynolds number R_B does not perform as well over the 20-35 μm radius range, as demonstrated by R^2 = 0.31 for the 25 μm particles (Fig. 8b). The better performance for smaller radii can find explanation in the information contained in R_B about the flow velocity and more specifically the turbulence intensity at the wind-wave boundary layer. We expect this to be key for the smaller droplets that are more subject to turbulent diffusion and less affected by gravitational settling than the larger spume droplets (e.g. Andreas et al. (2010)).

The scaling of spray concentrations by the wave slope variance $< S^2 >$ is presented in Figs. 7c and 8c. The most striking feature of these figures is the bahaviour for the intermediate wave forcing, which yields decreasing aerosol concentrations with $< S^2 >$, whereas the other types of forcing all yield increasing concentrations. This behaviour can be traced back to the earlier observation (Sect. 3.1) that the intermediate forcing yields a decrease in significant wave height with increasing $< S^2 >$ (and a less clear increase of $W(\%)$, which was attributed to (exceptionally) efficient wave energy dissipation that for the other three types of forcing. This contrasting behaviour for the intermediate forcing causes the overall fit quality for smaller particles to be less than when scaling with R_B (R^2 of 0.34 versus 0.49). Over the 20-35 μm range however, the wave slope variance offers the best scaling performance for all four scaling parameters (R^2 = 0.55). The wave slope variance thus appears

well adapted for the scaling of near-surface spume droplet concentrations (Fig. 8c).

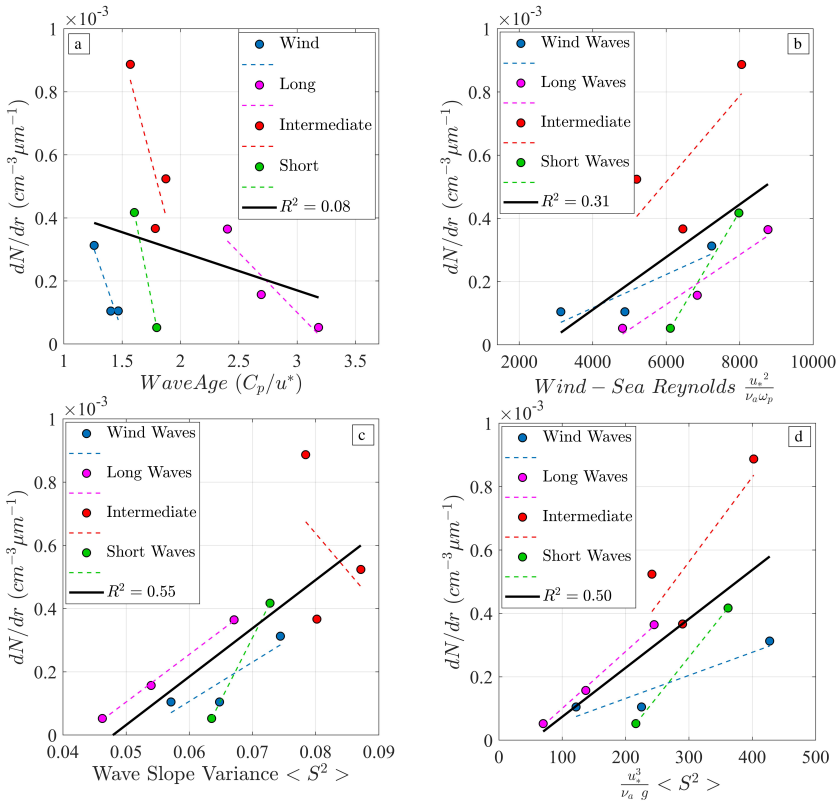

Fig. 8 Scaling of dN/dr with (a) wave age, (b) R_B, (c) $< S^2 >$ and (d) $P_S = \frac{u_*^3}{\nu_a g}.< S^2 >$ for particles of radius 25 μm, 35 cm above MWL. Individual wave forcings are denoted by colours, for U_{10} wind speeds ranging from 16 to 20 m s^{-1}. Solid black lines in all panels represent linear fits to all 12 datapoints.

Finally, we scale near-surface concentrations as a function of the combination of non-dimensional numbers $\frac{u_*^3}{\nu_a g}.< S^2 >$. Results show that the combined number P_S scales the particle concentrations better than either the wave age or the windsea Reynolds number. In comparison with the wave slope variance the combined number performance is better over the 7-20 μm range ($R^2 = 0.60$ versus $R^2 = 0.34$ for $r = 7.5$ μm), but about equal for particles greater than 20 μm ($R^2 = 0.5$ versus $R^2 = 0.55$ for $r = 25$ μm). However, the combined number results in similar trends for all four types of wave forcing, including

the intermediate forcing (compare panels c and d). This suggests that the combined number is capable of scaling sea spray generation for a wider range of environmental conditions than $< S^2 >$ alone. We therefore conclude that the combined number is well suited for the simultaneous scaling of breaking wave (bubble bursting) and surface tearing mechanisms.

4.4 Combined scaling parameters

Our fourth scaling parameter is similar to the non-dimensional numbers suggested by Brumer et al. (2017) and Lenain and Melville (2017). The latter authors combine the wave steepness, the wave age and a Reynolds number depending on the significant wave height H_s ($R_H = \frac{H_s u_*}{\nu}$). A similar number was also used by Brumer et al. (2017) for the scaling of whitecap coverage. Preliminary laboratory studies on the scaling of sea spray concentrations in the 7-35 μm radius range by the number proposed by Lenain and Melville (2017) suggest that the scaling does not significantly change when substituting R_H with R_B. However, significantly better scaling is achieved when the wave steepness ($H/2\lambda$) is replaced with $< S^2 >$.

As mentioned in the introduction, u_*^3 has proven to be a worthy candidate to scale wave energy dissipation and input from the wind field necessary for bubble and droplet production (Newell and Zakharov, 1992; Zhao and Toba, 2001; Zhao et al., 2006; Andreas, 1998, 2002; Fairall et al., 2009). Though not detailed in the present scaling analysis, a preliminary study allowed to evaluate the scaling performance of u_*^3 for near-surface concentrations. Results reveal similar performance to the combined number with good scaling results over the 7-20 μm range ($R^2 = 0.56$ for $r = 7.5$ μm) with less satisfactory performance for larger droplets ($R^2 = 0.23$ for $r = 25$ μm). Associating scaling performances

of u_*^3 (best for $r < 20$ μm) with $< S^2 >$ (best for $r > 20$ μm) in the combined number (Eq. 5) allows good scaling of sea spray aerosol generation over the 7-35 μm range, suggesting that the combination of both allows to scale production in a wider range of conditions than $< S^2 >$ alone.

4.5 The laboratory generation flux

In this section, we will consider a suitable scaling parameter for the spray generation flux (dF/dr). We will derive this flux from the sea spray concentration profiles measured in the laboratory (cf. Fig. 5), at each resolved particle size. We only use the data obtained for the higher wind speeds (16, 18 and 20 m s^{-1}), but we include all four types of wave forcing. As a first step we approach the vertical concentration profiles with a function depending on the natural logarithm of measurement height (cf. Sect. 4.1 and Fig. 5):

$$N^r(z) = N_*^r ln(z) + C^r \tag{6}$$

where radius-dependent the aerosol concentration at the surface N_*^r (m^{-3}) is determined by extending the measured aerosol concentration profiles to MWL. r denotes the dependence on the droplet radius. The sea spray flux dF/dr (m^{-2} s^{-1}) is subsequently obtained by multiplication with the friction velocity u_*:

$$\frac{dF}{dr} = N_*^r u_* \tag{7}$$

We evaluate N_*^r for each radius (bin) greater than 7 μm measured by our aerosol probes. This method is commonly used for the estimation of the sea spray flux in the field (Petelski et al., 2014), as well as for numerical LES (Large Eddy Simulation) data (Richter et al., 2019). However, the use of a logarithmic

function to describe the concentration gradient is debated, and other authors have prefered a power law (e.g., Fairall et al. (2009); Ortiz-Suslow et al. (2016)). Rather than entering this debate, we abide by the adequate fit of logarithmic functions to our data (cf. Fig. 5).

As discussed in the previous section, both the wave slope variance and the combined number are good candidates to scale droplet generation. The combined number is found suitable over the entire study radius range, and the wave slope variance for spume droplets. Thus, Figure 9 shows the size-dependent sea spray generation flux dF/dr (evaluated using Eq. 7) as function of both the combined number (panel (a)) and the wave slope variance (panel (b), for various representative droplet radii between 8.5 and 30 μm. Individual data for a specific radius was fitted to a power law presented as lines in Fig. 9. As expected, the figure demonstrates that the combined number and the wave slope variance are also good scaling parameters for the generation flux. In accordance with the positive slopes in Figs. 7 and 8 (panels c and d), increasing values of combined number or wave slope variance lead to a stronger flux. Although it is difficult to conclude visually from Fig. 9, a comparison of panels a and b reveals the better scaling performance of the combined number for smaller radii, as reflected in the quality of the fit for 8.5 particles μm. Finally, and interesting feature in both Figs. 9a and 9b is the increase in the curve slopes for increasing radius as function of the scaling parameters. The lower slopes are found for the larger droplets. These slopes, seem to converge towards a maximum slope in the jet droplet range as the curves become almost parallel for $r < 15$ μm. This suggests uneven radius-dependent flux strength variations over the sea spray spectrum according to the forcing.

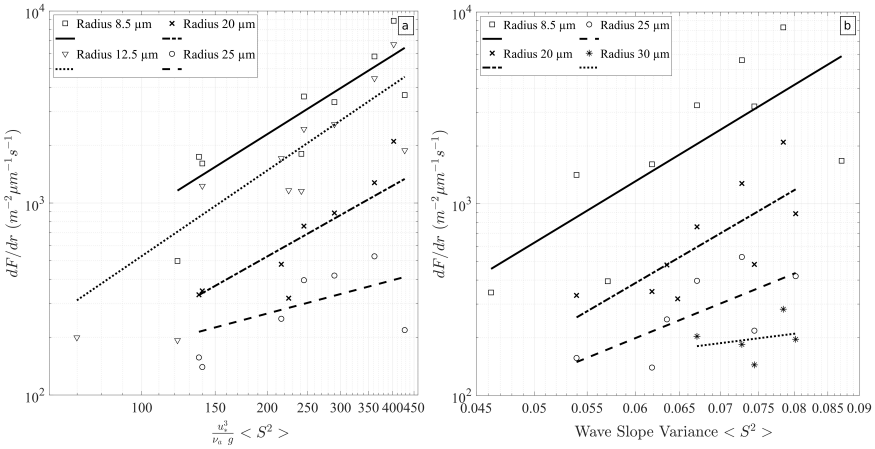

Fig. 9 The laboratory *dF/dr* sea spray flux as a function of (a) the combined number $\frac{u*^3}{\nu_a\, g} < S^2 >$ and (b) the wave slope variance $< S^2 >$. Lines denote power law fits to data for individual radii.

4.6 Comparison with other studies

This section presents a comparison of our generation flux to others reported in the literature. Since most existing fluxes rely on data acquired in the field, we must ascertain that our laboratory data can be compared to the field. Comparing air-sea interaction processes and resulting sea spray generation in laboratory conditions to the field is not a straightforward task, due to the greater complexity of the natural environment. It is important that physical mechanisms at play in the laboratory, as well as the resulting sea spray generation fluxes, be similar to those observed in the field. The former question has already been discussed in this paper; the wind flow (Sect. 2.4), the wave field (Sect. 3.1), and the whitecap coverage (Sect. 3.2) were all found to follow the same physics as in the field. As for the sea spray concentrations, Sect. 4.1 demonstrated the expected behaviour with increasing concentrations for increasing wind speed, a dependence on wave state, as well as a near-logarithmic

concentration profile later used to calculate the laboratory generation fluxes (Eqs. 6 and 7).

The above reasoning leads us to compare our laboratory sea spray generation flux to four (field and laboratory) flux formulations published in the literature. For this comparison we have evaluated our generation flux for the laboratory pure wind forcing for 18 probe size bins over the 5-30 μm radius range, with friction velocity $u_* = 1.05$ m s^{-1} and wind speed $U_{10} = 20$ m s^{-1} (cf. Table 1). The flux is depicted in Fig. 10 as the black solid line. The triangles denote the radii for which the dF/dr was evaluated, to which a polynomial function is fitted to facilitate comparison with the other generation spectra. Figure 10 also represents fluxes from the literature; Smith et al. (1993) denoted by S93 and the grey solid line, Andreas (1998) denoted by A98 and the dotted line, Laussac et al. (2018) denoted by L18 and the dashed line, and Fairall et al. (2009) denoted by F09 and the grey dashed line. The latter flux was obtained from laboratory data, the other three from field data. The Andreas (1998) and Smith et al. (1993) flux models solely depend on wind speed U_{10} and are evaluated here for $U_{10} = 20$ m s^{-1}. The F09 flux is estimated for $u_* = 1.35$ m s^{-1}, and is only valid for $r \geq 24$ μm. Finally, L18 flux strength depends on the whitecap coverage, in turn defined in terms of the wave age, and has a 0.5-20 μm radius validity range. The closest match with laboratory conditions (wave age equal to 1.25) was obtained by estimating the L18 flux for a wave age value of 3.9 using a fetch model adapted to the north-west Mediterranean (Lafon et al., 2004), corresponding with a MIRAMER campaign sample point located at 12 km fetch (Demoisson et al., 2013; Laussac et al., 2018) used to parameterise the L18 SSGF.

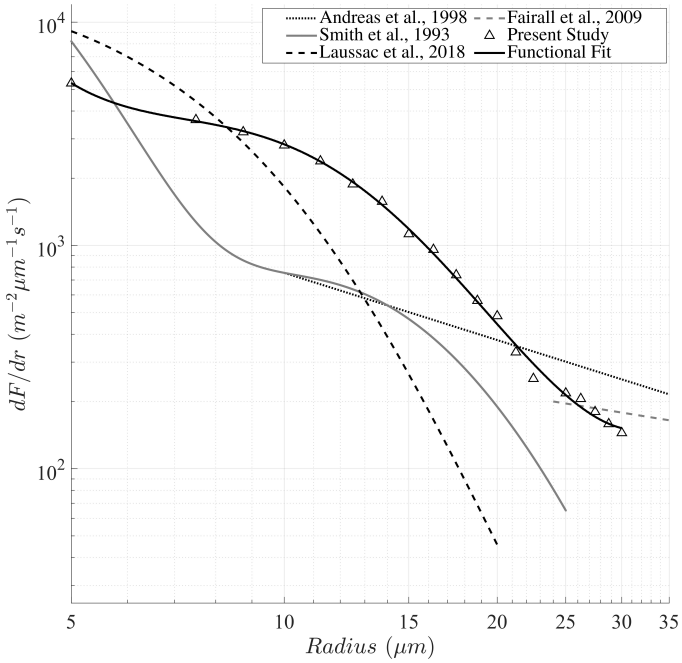

Fig. 10 Vertical sea spray concentration fluxes at $U_{10} = 20$ m s^{-1}.

Figure 10 shows that the various flux estimates have a spread of an order of magnitude. While this may seem significant, the spread is quite typical as evidenced by reviews of the various source functions reported over the years (Andreas, 1998; Lewis et al., 2004; Veron, 2015). Our flux function has the same strength as S93, A98 and L18 for particles of 5 μm, but suggests a stronger flux than these other functions as radius increases. Specifically, our flux curve includes a shoulder (or peak) around 10-15 μm, also seen in S93, which we attribute to a peak in jet droplet production. A similar shoulder is observed in the aerosol size distributions measured at 55 cm height above the surface (cf. Fig. 4). Moving forward to radii in excess of 15 μm, the typical domain of spume droplets, the strength of L18 and S93 generation functions decrease rapidly. In both cases, this decrease was attributed to an underestimation of

742 spume droplet production, for L18 because the experiment was hampered by
743 the near-absence of high wind speed events, and because for L18 and S93 the
744 height of the measurement towers prevented efficient dispersion of the spume
745 droplet location. In each case this can result in poor count statistics, and the
746 larger droplet concentrations are often discarded as done for r $>$ 35 μm in
747 the present study. Examples of efforts to compensate such effects include the
748 reformulation of S93 in A98, where the generation flux was corrected over the
749 spume droplet range (Andreas, 1998). For the larger radii (r $>$ 25 μm), our flux
750 function yields equal strength as F09. Because these largest particles reflect
751 the limits of our PMS probes it is difficult to conclude, but both our flux curve
752 and F09 seem to indicate that the decrease in strength becomes less strong
753 with radius. This may point to the presence of another shoulder around 30
754 μm, reflecting a peak in spume droplet generation.

755 5 Formulation of the new sea spray generation function

756 The previous sections demonstrated that the laboratory generation flux de-
757 pends on both wind and wave characteristics, with different responses for
758 individual radii. The dependence on radius is traditionally accounted for by
759 parameterising the SSGF with one or more modes centered around modal radii
760 (Monahan et al., 1986; Demoisson et al., 2013; Ovadnevaite et al., 2014; Laus-
761 sac et al., 2018). These modes can be represented with normal, log-normal,
762 or other distributions that are commonly used to reproduce measured aerosol
763 distribution characteristics. Modes are often associated with specific aerosol
764 processes, such as the generation of jet or spume droplets. We adopt this
765 methodology by introducing two modes at 7 and 25 μm radius, which we
766 consider representative for jet and spume droplets, respectively. The choice

of these centre radii was inspired by the shapes of the flux and concentration curves shown in Figs. 4 and 10, respectively. As mentioned in Sect. 2.5, we have excluded droplets with radii less than 7 μm radius for our analysis, but these droplets are evidently present in the tunnel (Fig. 4). On the basis of the shape of the aerosol size distribution shown in Fig. 4, we add a third mode centered around 2.5 μm. Taking 3 μm as the lower limit, the flux strength of the L18 SSGF is used over 3-7 μm. A smooth transition between the field-determined L18 and the laboratory data is attained by seeking a best fit between L18 flux distributions over the 3-7 μm range, and the laboratory flux distributions. The 7 μm radius marks the transition between both fluxes (cf. Fig. 11). To achieve this combination of flux functions, the whitecap coverage used in L18 (originally calculated from the wave age) (Laussac et al., 2018) is recalculated here as a function of present study scaling parameters (cf. Sect. 4.2). In the following, the L18 $W(\%)$ is estimated from $< S^2 >$ using Eq. 4. Section 4.3 revealed that the flux can be successfully scaled by a combined number P_S, but that the $< S^2 >$ also yields acceptable results, especially for larger particles. Therefore, we formulate two SSGFs in terms of three normally distributed modes, valid for droplets between 3-35 μm radius and wind speeds U_{10} ranging from 12-20 m s^{-1}:

$$\frac{dF_X}{dr_{80}} = \sum_{i=1}^{n} \frac{F_i(X)\tau^{-1}}{\sigma_i\sqrt{2\pi}} exp(-\frac{1}{2}(\frac{r_{80}-\mu_i}{\sigma_i})^2) \quad (8)$$

where X is the scaling parameter (P_S or $< S^2 >$), r_{80} is the particle radius at $RH = 80\%$, $\frac{dF_X}{dr_{80}}$ is the size dependent SSGF determined from environmental parameters contained in $F_i(X)$, and τ is the whitecap decay rate. μ_i and σ_i are the mean radius and standard deviation of each of the three modes. The SSGFs can be given in terms of r_{80}, because the underlying laboratory data was obtained for 80% humidity (cf. the discussion in Sect. 2.5). In formulating the SSGFs, we found best results were obtained using normal modes, whereas other

authors have preferred lognormal modes (e.g. Ovadnevaite et al. (2014)). Possibly, this signals that normal modes are more suitable for the larger droplets studied here. Numerical values for Eq. 8 are specified in Table 2. In addition, the whitecap decay rate was given a value of 3.53 (Laussac et al., 2018). Despite a focus on the 16-20 m s^{-1} range in Sect. 4, we are confident that the SSGFs are valid over the 12-20 m s^{-1} range as a result of the strong relationship between numbers $< S^2 >$ and P_S and the physical mechanisms known to drive production (cf. sects. 2.4 and 3.2) for these wind speeds.

Table 2 shows that flux amplitudes are expressed as power laws of $< S^2 >$ and P_S, as suggested with the apparent power law behaviour between scaling parameters and fluxes presented in Fig. 9.

Table 2 Parameters for the two SSGFs.

i	σ_i	μ_i	$F_i(\frac{u*^3}{\nu_a g} < S^2 >)$	$F_i(< S^2 >)$
1	2.1	2.5	$4.37 \times 10^2(\frac{u*^3}{\nu_a g} < S^2 >)^{0.92}$	$4.94 \times 10^7(< S^2 >)^{2.45}$
2	7	7	$6.84 \times 10^1(\frac{u*^3}{\nu_a g} < S^2 >)^{1.41}$	$7.88 \times 10^7(< S^2 >)^{2.3}$
3	12	25	$4.75 \times 10^1(\frac{u*^3}{\nu_a g} < S^2 >)^{1.11}$	$1.3 \times 10^7(< S^2 >)^{2.39}$

The two new SSGFs are presented in Figure 11 as two series of solid lines, where panels a and b denote results for the SSGF in terms of the combined number P_S and $< S^> $ respectively. These lines are colour-coded according to the values of the scaling parameters; the colour scale is indicated on the right of the individual panels. The range of values was chosen to correspond with the laboratory configurations for all types of wind speeds between 16 and 20 m s^{-1}. The experimental flux data obtained in these configurations is visualised by the color-coded plus signs in Fig. 11. Finally, Figure 11 also presents the flux spectra prescribed by the L18 SSGF (Laussac et al., 2018) over the 3-7 μm range, which, as mentioned above, was modified so that the whitecap coverage $W(\%)$ scaling parameter (originally calculated from the wave age),

was recalculated to depend on either P_S or $< S^2 >$. The recalculated L18 flux spectra are represented by the color-coded dashed lines.

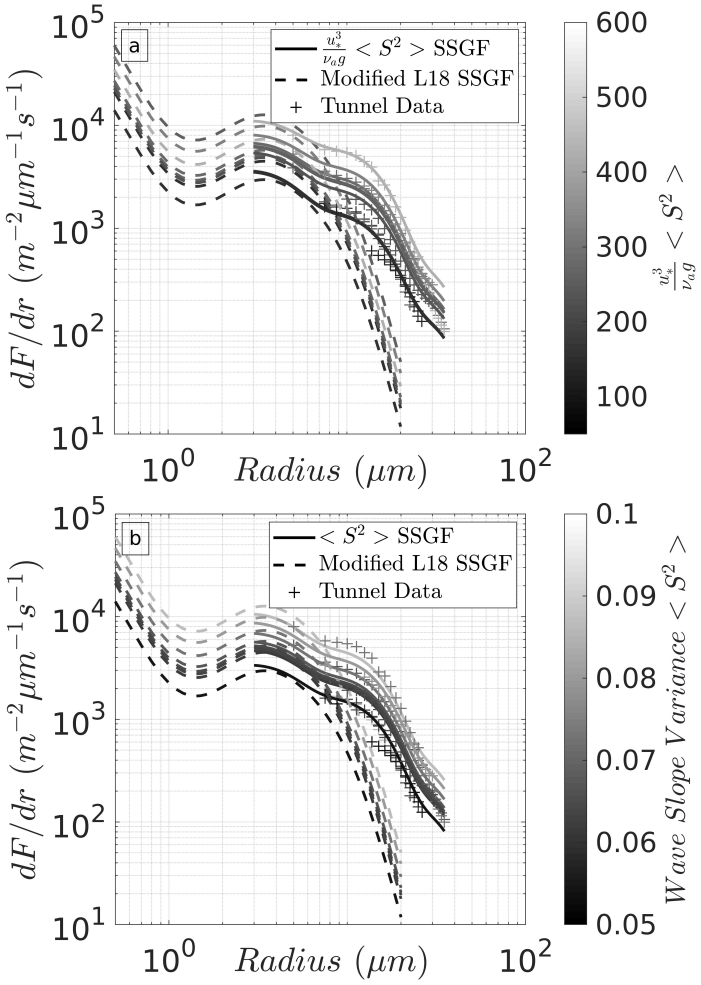

Fig. 11 The altered L18 SSGF (dashed lines) and the (a) combined number P_S and (b) wave slope variance $< S^2 >$ SSGFs. Line colors depend on respective non-dimensional (a) P_S and (b) $< S^2 >$ values.

Figure 11 demonstrates that the two SSGFs reproduce the experimental flux data obtained in the tunnel quite well, although differences of up to a factor 2 remain. In view of the already noted significant spread in individual flux functions reported in the literature (Tsyro et al., 2011; Chen et al., 2016; Neumann et al., 2016), we consider this performance adequate. The figure

822 also demonstrates that the two modes at 7 and 25 μm adequately reproduce
823 the shape of the tunnel spectra, and this better than flux functions with less
824 modes in the large particle size domain (e.g., S93 and L18). Finally, Fig. 11
825 also shows that both SSGFs connect reasonably well to L18. While this was
826 expected with a 2.5 μm mode inspired by L18 flux strengths, this result offers
827 a perpective for a future coupling between the new SSGFs and L18, thereby
828 extending a universal function to the 0.1-35 μm range. These results also offer
829 a perspective for future improvements on the combination of laboratory and
830 field sea spray measurements.

831 6 Discussion and conclusion

832 6.1 Generation mechanisms

833 The aim of this study is to investigate the sea spray generation processes for
834 different wind and wave combinations. We performed our studies in a wave-
835 wind interaction laboratory and thus, our first task was to demonstrate that
836 important generation mechanisms such as wave breaking (cf. Sect. 3.2) and
837 airflow characteristics (cf. Sect. 2.4) are similar in the laboratory and in the
838 field. Sea spray concentrations over the 7-35 μm radius range are found to
839 depend on both wind speed and the sea state, and are found to decrease near-
840 logarithmically for increasing distance from the water surface. The concentra-
841 tion spectra (Fig. 4) exhibit peaks at approximately 2.5 and 7 μm similar to
842 observations in the field (Laussac et al., 2018), attributed to regimes of film
843 and and jet droplet generation predominance, respectively. A third peak was
844 identified from the volume concentration spectra (Fig. 6) and corresponds to
845 the spume droplet size range. This peak was absent for wind speeds under 12 m

s^{-1} (Sect. 4.1), in accordance with the threshold for spume droplet production (Monahan et al., 1986; Andreas et al., 2010). The larger droplet concentrations are found in conditions with high values for whitecap coverage and wave slope variance. These conditions correspond to intermediate and short wave forcing in the laboratory (cf. Table 1). In contrast, long wave forcing or forcing by wind alone result in lower concentrations.

6.2 Scaling sea spray generation with $< S^2 >$

The sea spray generation flux is calculated assuming logarithmic concentration profiles (Sect. 4.5), motivated by the near-logarithmic profiles obtained in the laboratory (Fig. 5). The sea spray generation is scaled against four parameters that reflect the wind-wave conditions: wave age, windsea Reynolds number R_B, wave slope variance $< S^2 >$, and a combined number $\frac{u*^3}{\nu_a g} < S^2 >$, denoted P_S, describing the wave slope variance-modulated wind energy input to the waves. Whilst the wave age is a useful heuristic tool to estimate wave-wind equilibria, our results indicate that it does not allow satisfactory scaling of sea spray generation for different wind and wave combinations (cf. Figs. 7 and 8). The windsea Reynolds number R_B, also combining wind and peak wave characteristics, provides good results for smaller droplets (7-20 μm range), comparable to the performance for $< S^2 >$. However, $< S^2 >$ significantly outperforms R_B for spume droplets with radii greater than 20 μm (cf. Fig. 8). This difference may be expected because R_B only includes information about peak wave statistics, whereas $< S^2 >$ is related to turbulence strength at the air-sea interface and wave breaking phenomena on a range of spatial scales. This is in agreement with an increasing number of microphysical studies that relate wave slope to turbulent events such as airflow separation and wind shear,

which are thought to drive the surface tearing of spume droplets at the wave crests (Banner and Melville, 1976; Kawai, 1981; Reul et al., 2008; Mueller and Veron, 2014; Buckley and Veron, 2019).

Of the four tested scaling parametersn the combined number P_S gives the best overall performance: it is particularly well suited for the scaling of sea spray generation for radii in the 7-20 μm range, where bubble bursting generation dominates, but the larger spume droplets are also well scaled. The spume droplet scaling performance reflects the presence of $< S^2 >$, and the scaling performance for smaller droplets may be attributed to u_*^3 as a result of its well documented relationship with wave energy dissipation. The concept of combined scaling parameters has also been explored by other authors (Brumer et al., 2017; Lenain and Melville, 2017) (cf. Sect. 4.4). A comparative study (Sect. 4.3) shows that minor differences in the definition of the combined number (e.g. by using a Reynolds number defined in terms of significant wave height) do not impact on the performance, in contrast to the significant difference obtained when replacing wave steepness with the multiscale wave slope variance.

From a practical point of view, it is interesting to compare scaling performance to the difficulty to measure the scaling parameters. Both wave age and the windsea Reynolds number R_B require a wind parameter and relatively common wave parameters. The wave age does not scale the flux properly for the range of tested forcings, and R_B scaling performances are mainly limited to the smaller jet droplet particles. The measurement difficulty increases when considering the multiscale information (wave spectrum) required for $< S^2 >$, and the combined number P_S adds further complexity by requiring the wind friction velocity u_*. The use of approximate equations to estimate $< S^2 >$ from

more readily-accessible parameters (e.g. Eqs. 3 and 4) may thus be considered, albeit with loss of scaling performance.

6.3 $< S^2 >$ and traditional scaling parameters

As mentioned in the previous section, it may be difficult to measure $< S^2 >$ in the field. The use of the approximate equations to infer $< S^2 >$ from more accessible parameters such as wind speed U_{10} (Eq. 3), or whitecap coverage $W(\%)$ (Eq. 4) may then be considered, as the wave slope variance $< S^2 >$ has often been considered proportional to both the wind speed at U_{10} and the friction velocity u_* (Cox and Munk, 1956; Lenain et al., 2019). In a similar fashion, tt is important to note that many authors obtain $W(\%)$ from wind speed Monahan and Muircheartaigh (1980). Though not explicitly presented here, $\frac{u*^3}{\nu_a g} < S^2 >$ and $< S^2 >$ (and to a lesser extent R_B) outperform the measured U_{10}, u_* and $W(\%)$ for the scaling of sea spray generation in the tested laboratory configurations, especially for larger droplets. $W(\%)$ presents R^2 values ranging between 0.2 and 0.45 over the 7-35 μm range, with best results over the jet droplet range. U_{10} and u_* scaling performances are lower than for $W(\%)$ overall, except for the smaller radii of the jet droplet range where U_{10} and u_* show good correlation with spea spray generation, with R^2 values reaching maxima of 0.49 and 0.54 (for $r = 7$ μm), respectively. These better results over the jet droplet range are coherent with the performances of the combined number P_S with the u_*^3 term. Furthermore, this shows that $< S^2 >$ carries additional information (despite the good correlation between $< S^2 >$ and $W(\%)$ - cf. Eq. 4) about the wave field relative to these three parameters, such as the presumed role of the wave slope in the modulation of the air flow and surface tearing mechanisms, as discussed in Sect 4.1.

Unlike $< S^2 >$, U_{10} and u_* are not found to be appropriate tools for the upscaling and extrapolation of sea spray generation and whitecap coverage from the laboratory to the field, similar to observations made by Toba et al. (2006) when comparing tunnel and field data. Altough $< S^2 >$ outperforms U_{10} and u_*, there are conditions in which the wind parameters scale the aerosol concentrations as successfully. This pertains to smaller droplets (r < 12.5 μm) and relatively low wind speeds of 8 and 12 m s^{-1}, and a wave field that is forced by the wind. In these circumstances, sea spray consists almost exclusively of the bubble-mediated jet droplets produced from breaking waves under conditions of strong wave-wind equilibrium. Further analysis of our laboratory data reveals that the linear relation between U_{10} and $< S^2 >$ presented by Cox and Munk (1956) (Eq. 3) is best observed for the conditions corresponding to pure wind forcing. This is coherent with the good scaling performance of U_{10} and u_* under these conditions, as mentioned above. However, notable deviations from this linear relationship are observed with other types of wave forcing, which we attribute to the sensitivity of $< S^2 >$ to wave-wind equilibria (quantified here with wave age). The monochromatic properties of the longer wave conditions that experience less wind forcing, resulting in low wave energy at the higher frequencies of the wave spectrum, thereby affecting the value of $< S^2 >$. In this respect, a future laboratory study with more realistic wave fields such as the JONSWAP spectra (Hasselmann et al., 1973) would be worthwhile.

6.4 Validation against field data

The sea spray generation fluxes measured in the laboratory are compared to other existing source functions obtained in the field and in laboratory conditions. Our data compare favourably with the SPANDEX laboratory data

reported by Fairall et al. (2009). Flux estimates differ typically by less than an order of magnitude when compared to flux functions obtained in the field (Smith et al., 1993; Andreas, 1998), which is in accordance with the typical spread in the literature (Andreas, 1998; Veron, 2015). More substantial differences are noted from the spume droplet domain, when we compare our flux estimates to a function that does not accommodate these large particles explicitly (Laussac et al., 2018). These results prove that the laboratory is a good instrument for determining generation fluxes. This inspires us to continue the tunnel experiments, since the tunnel is better suited for the study of sea spray production for a wide range of wave fields and in high winds representative of extreme events. Also, the tunnel facilitates the complex experiments required to understand the generation processes at the microphysical scale, such as airflow separation, and the effects of sea spray on heat, moisture and momentum fluxes at the air-sea interface. Ideally, such experiments should be performed with salt water, for easier comparison with field experiments, because saltwater and freshwater lead to differences in the aerosol concentrations and distributions (Fairall et al., 2009; Mehta et al., 2019).

6.5 Sea spray generation functions (SSGFs) derived from laboratory experiments

The laboratory experiments culminated in two sea spray generation functions (SSGFs) (cf. Fig. 11 and Table 2). These SSGFs describe the droplet generation spectrum as a sum of three normally distributed modes, and are validated for wind speeds ranging from 12-20 m s^{-1} and droplet radii 3-35 μm. The radius range spans the major part of the film and jet ranges, as well as an appreciable start of the spume droplet range. One SSGF solely dependent on the wave

slope variance, and to our knowledge is the first of its kind. Wave slope variance measurements in the field are scarce, and for practical purposes it may be necessary to estimate the wave slope variance from more readily available variables such as wind speed (Eq. 3, Cox and Munk (1956)), or from measured or modelled wave spectra (Elfouhaily et al., 1997). As shown in Section 6.3, such approximations may reduce the accuracy of the SSGF. The second SSGF depends on a combined scaling parameter in terms of both $< S^2 >$ and u_*^3. Though obtaining accurate measurements or predictions of u_*^3 may be challenging in the field (and thus renders the use of the second SSGF even more difficult than the one depending solely on $< S^2 >$), this non-dimensional number is undeniably the best scaling tool for the generation of film and jet droplets, and also scales the larger spume droplets satisfactorily. In extrapolating the P_S-dependent SSGF down to 12 m s^{-1} the flux may be underestimated at these lower wind speeds, following the suggestion by Andreas (1998) that the rate of spume droplet generation increases with u_*^2 and not u_*^3 for winds below 15 m s^{-1}.

6.6 Outlook

Recent improvements in the integration of higher order wave field properties in numerical wave models (Cathelain, 2017) and the coupling of wave, atmospheric and circulation models (Pianezze et al., 2018) provide an impetus for the study of sea spray generation processes. Present study results have shown that the integration of the wave field is essential for the better scaling of the sea spray generation. As we work towards universal SSGFs valid for a wide range of (complex) environmental conditions, a further understanding is required of the effect of multiscale (i.e. millimeter to meter scale) boundary processes

sea spray fluxes. This may include first and higher order statistics, such as for the consideration of overlapping wave fields, the directional spreading of wave spectra (Peureux et al., 2018) and wave-current interactions affecting surface wave properties (Ardhuin et al., 2017). As the present study has highlighted the importance of the wave slope variance in modelling droplet fluxes, we signal an urgent need for a better understanding of small-scale sea surface characteristics (Jähne and Riemer, 1990). Unfortunately, field measurements of these characteristics have been relatively sparse (Munk, 2009), not in the least because the spatial resolution of airborne and satellite-based sensors is limited and the presence of whitecaps complicates the retrieval of slope variance estimates (Cox and Munk, 1956; Lenain et al., 2019).

Finally, having demonstrated that the tunnel is a good proxy to the field in determining sea spray fluxes, we would now like to extend the comparison to the aerosol concentrations at some height above the water surface. However, this is not a simple task since the differences in dispersion characteristics, background concentrations and production footprints between the tunnel and the field need to be elucidated. Efforts to do so are underway, and will be reported elsewhere.

Acknowledgements

A special thanks to engineer Rémi Chemin (University of Toulon) for his thoughts and contribution during the laboratory experiment. We are grateful for the sponsorship by the Agence Innovation Défense (AID-DGA) under contract 2018-60-0038 and the Region SUD contract 2018-06085. This work also benefitted from the MATRAC research effort sponsored by ANR-ASTRID under contract ANR-18-ASTR-0002.

References

Andreas EL (1989) Thermal and size evolution of sea spray droplets. Cold Regions Research and Engineering Lab Hanover NH, Tech rep

Andreas EL (1992) Sea spray and the turbulent air-sea heat fluxes. Journal of Geophysical Research: Oceans 97(C7):11,429–11,441, DOI 10.1029/92JC00876

Andreas EL (1998) A new sea spray generation function for wind speeds up to 32 m s1. Journal of Physical Oceanography 28(11):2175–2184, DOI 10.1175/1520-0485(1998)028⟨2175:ANSSGF⟩2.0.CO;2

Andreas EL (2002) A review of the sea spray generation function for the open ocean. Advances in Fluid Mechanics 33:1–46

Andreas EL, Jones KF, Fairall CW (2010) Production velocity of sea spray droplets. Journal of Geophysical Research: Oceans 115(C12)

Anguelova M, Barber RP, Wu J (1999) Spume drops produced by the wind tearing of wave crests. Journal of Physical Oceanography 29(6):1156–1165, DOI 10.1175/1520-0485(1999)029⟨1156:SDPBTW⟩2.0.CO;2

Ardhuin F, Gille ST, Menemenlis D, Rocha CB, Rascle N, Chapron B, Gula J, Molemaker J (2017) Small-scale open ocean currents have large effects on wind wave heights. Journal of Geophysical Research: Oceans 122(6):4500–4517

Banner ML, Melville WK (1976) On the separation of air flow over water waves. Journal of fluid mechanics 77(4):825–842

Banner ML, Gemmrich JR, Farmer DM (2002) Multiscale measurements of ocean wave breaking probability. Journal of physical oceanography 32(12):3364–3375

Blanchard DC (1963) The electrification of the atmosphere by particles from bubbles in the sea. Progress in oceanography 1:73–202

Bringer A, Chapron B, Mouche A, Guérin CA (2013) Revisiting the short-wave spectrum of the sea surface in the light of the weighted curvature approximation. IEEE transactions on geoscience and remote sensing 52(1):679–689

Brumer SE, Zappa CJ, Brooks IM, Tamura H, Brown SM, Blomquist BW, Fairall CW, Cifuentes-Lorenzen A (2017) Whitecap coverage dependence on wind and wave statistics as observed during so gasex and hiwings. Journal of Physical Oceanography 47(9):2211–2235

Buckley MP, Veron F (2019) The turbulent airflow over wind generated surface waves. European Journal of Mechanics-B/Fluids 73:132–143

Callaghan AH, Deane GB, Stokes MD, Ward B (2012) Observed variation in the decay time of oceanic whitecap foam. Journal of Geophysical Research: Oceans 117(C9)

Canepa E, Builtjes PJ (2017) Thoughts on earth system modeling: From global to regional scale. Earth-Science Reviews 171:456–462

Cathelain M (2017) Development of a deterministic numerical model for the study of the coupling between an atmospheric flow and a sea state. PhD thesis, Ecole Centrale de Nantes (ECN)

Chen Y, Cheng Y, Ma N, Wolke R, Nordmann S, Schüttauf S, Ran L, Wehner B, Birmili W, van der Gon HA, et al. (2016) Sea salt emission, transport and influence on size-segregated nitrate simulation: a case study in northwestern europe by wrf-chem

Cipriano RJ, Blanchard DC (1981) Bubble and aerosol spectra produced by a laboratory breaking wave. Journal of Geophysical Research: Oceans 86(C9):8085–8092

Coantic M, Ramamonjiarisoa A, Mestayer P, Resch F, Favre A (1981) Wind-water tunnel simulation of small-scale ocean-atmosphere interactions. Journal of Geophysical Research: Oceans 86(C7):6607–6626

1076 Cox C, Munk W (1956) Slopes of the sea surface deduced from photographs
1077 of sun glitter
1078 De Leeuw G (1986) Vertical profiles of giant particles close above the sea
1079 surface. Tellus B 38(1):51–61
1080 De Leeuw G, Andreas EL, Anguelova MD, Fairall C, Lewis ER, O'Dowd C,
1081 Schulz M, Schwartz SE (2011) Production flux of sea spray aerosol. Reviews
1082 of Geophysics 49(2)
1083 Demoisson A, Tedeschi G, Piazzola J (2013) A model for the atmospheric
1084 transport of sea-salt particles in coastal areas. Atmospheric research
1085 132:144–153
1086 Duncan J (1981) An experimental investigation of breaking waves produced
1087 by a towed hydrofoil. Proceedings of the Royal Society of London A Math-
1088 ematical and Physical Sciences 377(1770):331–348
1089 van Eijk AM, Tranchant BS, Mestayer PG (2001) Seacluse: Numerical simu-
1090 lation of evaporating sea spray droplets. Journal of Geophysical Research:
1091 Oceans 106(C2):2573–2588
1092 Elfouhaily T, Chapron B, Katsaros K, Vandemark D (1997) A unified direc-
1093 tional spectrum for long and short wind-driven waves. Journal of Geophys-
1094 ical Research: Oceans 102(C7):15,781–15,796
1095 Fairall C (1990) Modelling the fate and influence of marine spray. Modelling
1096 the Fate and Influence of Marine Spray,(Eds P Mestayer, EC Monahan, and
1097 PA Beetham) Whitecap Rep'l, University of Connecticut, Marine Sciences
1098 Institute, Groton, pp I-5
1099 Fairall C, Banner M, Peirson W, Asher W, Morison R (2009) Investigation
1100 of the physical scaling of sea spray spume droplet production. Journal of
1101 Geophysical Research: Oceans 114(C10)
1102 Frick G, Hoppel W (2000) Airship measurements of ships exhaust plumes and
1103 their effect on marine boundary layer clouds. Journal of the atmospheric

sciences 57(16):2625–2648

Hasselmann K, Barnett T, Bouws E, Carlson H, Cartwright D, Enke K, Ewing J, Gienapp H, Hasselmann D, Kruseman P, et al. (1973) Measurements of wind-wave growth and swell decay during the joint north sea wave project (jonswap). Ergänzungsheft 8-12

Holmes P, Lumley JL, Berkooz G (1996) Turbulence, Coherent Structures, Dynamical Systems and Symmetry. Cambridge Monographs on Mechanics, Cambridge University Press, DOI 10.1017/CBO9780511622700

Holthuijsen L, Herbers T (1986) Statistics of breaking waves observed as whitecaps in the open sea. Journal of Physical Oceanography 16(2):290–297

Husain NT, Hara T, Buckley MP, Yousefi K, Veron F, Sullivan PP (2019) Boundary layer turbulence over surface waves in a strongly forced condition: Les and observation. Journal of Physical Oceanography 49(8):1997–2015

Iida N, Toba Y, Chaen M (1992) A new expression for the production rate of sea water droplets on the sea surface. Journal of Oceanography 48(4):439–460

Jaenicke R (1984) Physical aspects of atmospheric aerosol in aerosols and their climatic effects;(eds) he gerbard and a deepak

Jähne B, Riemer KS (1990) Two-dimensional wave number spectra of small-scale water surface waves. Journal of Geophysical Research: Oceans 95(C7):11,531–11,546

Johansson JH, Salter ME, Navarro JA, Leck C, Nilsson ED, Cousins IT (2019) Global transport of perfluoroalkyl acids via sea spray aerosol. Environmental Science: Processes & Impacts 21(4):635–649

Kawai S (1981) Visualization of airflow separation over wind-wave crests under moderate wind. Boundary-Layer Meteorology 21(1):93–104

Lafon C, Piazzola J, Forget P, Le Calve O, Despiau S (2004) Analysis of the variations of the whitecap fraction as measured in a coastal zone. Boundary-

1132 layer meteorology 111(2):339–360
1133 Lafon C, Piazzola J, Forget P, Despiau S (2007) Whitecap coverage in coastal
1134 environment for steady and unsteady wave field conditions. Journal of ma-
1135 rine systems 66(1-4):38–46
1136 Laussac S, Piazzola J, Tedeschi G, Yohia C, Canepa E, Rizza U, Van Eijk A
1137 (2018) Development of a fetch dependent sea-spray source function using
1138 aerosol concentration measurements in the north-western mediterranean.
1139 Atmospheric Environment 193:177–189
1140 Lenain L, Melville WK (2017) Evidence of sea-state dependence of aerosol
1141 concentration in the marine atmospheric boundary layer. Journal of Physical
1142 Oceanography 47(1):69–84
1143 Lenain L, Statom NM, Melville WK (2019) Airborne measurements of surface
1144 wind and slope statistics over the ocean. Journal of Physical Oceanography
1145 49(11):2799–2814
1146 Lewis ER, Lewis ER, Lewis R, Karlstrom KE, Schwartz SE (2004) Sea salt
1147 aerosol production: mechanisms, methods, measurements, and models, vol
1148 152. American Geophysical Union
1149 Mallet M, Roger J, Despiau S, Dubovik O, Putaud J (2003) Microphysical
1150 and optical properties of aerosol particles in urban zone during escompte.
1151 Atmospheric Research 69(1-2):73–97
1152 Mårtensson E, Nilsson E, de Leeuw G, Cohen L, Hansson HC (2003) Lab-
1153 oratory simulations and parameterization of the primary marine aerosol
1154 production. Journal of Geophysical Research: Atmospheres 108(D9)
1155 Mehta S, Ortiz-Suslow DG, Smith A, Haus B (2019) A laboratory investiga-
1156 tion of spume generation in high winds for fresh and seawater. Journal of
1157 Geophysical Research: Atmospheres 124(21):11,297–11,312
1158 Monahan E, Spiel D, Davidson K (1986) A model of marine aerosol generation
1159 via whitecaps and wave disruption. In: Oceanic whitecaps, Springer, pp 167–

174

Monahan EC, Muircheartaigh I (1980) Optimal power-law description of oceanic whitecap coverage dependence on wind speed. Journal of Physical Oceanography 10(12):2094–2099

Monin AS, Obukhov AM (1954) Basic laws of turbulent mixing in the surface layer of the atmosphere. Contrib Geophys Inst Acad Sci USSR 151(163):e187

Mueller JA, Veron F (2009) A sea state–dependent spume generation function. Journal of physical oceanography 39(9):2363–2372

Mueller JA, Veron F (2014) Impact of sea spray on air–sea fluxes. part i: Results from stochastic simulations of sea spray drops over the ocean. Journal of Physical Oceanography 44(11):2817–2834

Mulcahy J, O'Dowd C, Jennings S, Ceburnis D (2008) Significant enhancement of aerosol optical depth in marine air under high wind conditions. Geophysical Research Letters 35(16)

Munk W (2009) An inconvenient sea truth: Spread, steepness, and skewness of surface slopes. Annual review of marine science 1:377–415

Neumann D, Matthias V, Bieser J, Aulinger A, Quante M (2016) A comparison of sea salt emission parameterizations in northwestern europe using a chemistry transport model setup. Atmospheric Chemistry and Physics (ACP) 16:9905–9933

Newell AC, Zakharov VE (1992) Rough sea foam. Physical review letters 69(8):1149

Newitt D (1954) Liquid entrainment 1. the mechanism of drop formation from gas vapour bubbles. Trans Instn Chem Engrs 32:244–261

Ortiz-Suslow D, Haus BK, Mehta S, Laxague N (2016) A laboratory study of spray generation in high winds. In: IOP Conference Series: Earth and Environmental Science, IOP Publishing, vol 35, p 012008

1187 Ovadnevaite J, de Leeuw G, Ceburnis D, Monahan C, Partanen AI, Korho-
1188 nen H, O'Dowd C, et al. (2014) A sea spray aerosol flux parameterization
1189 encapsulating wave state. Atmospheric Chemistry and Physics 14(4):1837
1190 Petelski T, Markuszewski P, Makuch P, Jankowski A, Rozwadowska A (2014)
1191 Studies of vertical coarse aerosol fluxes in the boundary layer over the baltic
1192 sea. Oceanologia 56(4):697–710
1193 Peureux C, Benetazzo A, Ardhuin F (2018) Note on the directional properties
1194 of meter-scale gravity waves. Ocean Science 14(1):41–52
1195 Pianezze J, Barthe C, Bielli S, Tulet P, Jullien S, Cambon G, Bousquet O,
1196 Claeys M, Cordier E (2018) A new coupled ocean-waves-atmosphere model
1197 designed for tropical storm studies: example of tropical cyclone bejisa (2013–
1198 2014) in the south-west indian ocean. Journal of Advances in Modeling
1199 Earth Systems 10(3):801–825
1200 Piazzola J, Despiau S (1998) Vertical variation of extinction and atmospheric
1201 transmission due to aerosol particles close above the sea surface in the
1202 mediterranean coastal zone. Optical Engineering 37
1203 Piazzola J, Mihalopoulos N, Canepa E, Tedeschi G, Prati P, Zarmpas P, Bas-
1204 tianini M, Missamou T, Cavaleri L (2016) Characterization of aerosols above
1205 the northern adriatic sea: Case studies of offshore and onshore wind condi-
1206 tions. Atmospheric Environment 132:153–162
1207 Plant WJ (1982) A relationship between wind stress and wave slope. Journal
1208 of Geophysical Research: Oceans 87(C3):1961–1967
1209 Pope SB (2000) Turbulent Flows. Cambridge University Press, DOI 10.1017/
1210 CBO9780511840531
1211 Pruppacher HR, Klett J (1978) Microphysics of clouds and precipitation reidel.
1212 Dordrecht, The Netherlands
1213 Ramberg SE, Griffin OM (1987) Laboratory study of steep and breaking deep
1214 water waves. Journal of waterway, port, coastal, and ocean engineering

113(5):493–506

Reul N, Branger H, Giovanangeli JP (2008) Air flow structure over short-gravity breaking water waves. Boundary-layer meteorology 126(3):477–505

Richter DH, Dempsey AE, Sullivan PP (2019) Turbulent transport of spray droplets in the vicinity of moving surface waves. Journal of Physical Oceanography 49(7):1789–1807

Savelyev I, Anguelova M, Frick G, Dowgiallo D, Hwang P, Caffrey P, Bobak J (2014) On direct passive microwave remote sensing of sea spray aerosol production. Atmospheric Chemistry and Physics 14(21):11,611

Schwendeman M, Thomson J (2015) Observations of whitecap coverage and the relation to wind stress, wave slope, and turbulent dissipation. Journal of Geophysical Research: Oceans 120(12):8346–8363

Sellegri K, O'Dowd C, Yoon Y, Jennings S, de Leeuw G (2006) Surfactants and submicron sea spray generation. Journal of Geophysical Research: Atmospheres 111(D22)

Smith M, Park P, Consterdine I (1993) Marine aerosol concentrations and estimated fluxes over the sea. Quarterly Journal of the Royal Meteorological Society 119(512):809–824

Spiel DE (1994) The sizes of the jet drops produced by air bubbles bursting on sea-and fresh-water surfaces. Tellus B: Chemical and physical meteorology 46(4):325–338

Stokes GG (1880) Supplement to a paper on the theory of oscillatory waves. Mathematical and Physical papers 1(314-326):14

Toba Y, Koga M (1986) A parameter describing overall conditions of wave breaking, whitecapping, sea-spray production and wind stress. 37-47

Toba Y, Komori S, Suzuki Y, Zhao D (2006) Similarity and dissimilarity in air-sea momentum and co2 transfers: the nondimensional transfer coefficients in light of windsea reynolds number. Atmosphere-ocean interactions 2:53–82

1243 Troitskaya Y, Kandaurov A, Ermakova O, Kozlov D, Sergeev D, Zilitinkevich
1244 S (2018) The bag breakup spume droplet generation mechanism at high
1245 winds. part i: Spray generation function. Journal of Physical Oceanography
1246 48(9):2167–2188
1247 Tsyro S, Aas W, Soares J, Sofiev M, Berge H, Spindler G (2011) Modelling of
1248 sea salt concentrations over europe: key uncertainties and comparison with
1249 observations
1250 Vandemark D, Chapron B, Sun J, Crescenti GH, Graber HC (2004) Ocean
1251 wave slope observations using radar backscatter and laser altimeters. Journal
1252 of Physical Oceanography 34(12):2825–2842
1253 Veron F (2015) Ocean spray. Annual Review of Fluid Mechanics 47:507–538
1254 Veron F, Hopkins C, Harrison E, Mueller J (2012) Sea spray spume droplet
1255 production in high wind speeds. Geophysical Research Letters 39(16)
1256 Woolf DK (1997) Bubbles and their role in gas exchange. The sea surface and
1257 global change
1258 Wu J (1993) Production of spume drops by the wind tearing of wave crests:
1259 The search for quantification. Journal of Geophysical Research: Oceans
1260 98(C10):18,221–18,227
1261 Yoon Y, Ceburnis D, Cavalli F, Jourdan O, Putaud J, Facchini M, Decesari S,
1262 Fuzzi S, Sellegri K, Jennings S, et al. (2007) Seasonal characteristics of the
1263 physicochemical properties of north atlantic marine atmospheric aerosols.
1264 Journal of Geophysical Research: Atmospheres 112(D4)
1265 Zhao D, Toba Y (2001) Dependence of whitecap coverage on wind and wind-
1266 wave properties. Journal of oceanography 57(5):603–616
1267 Zhao D, Toba Y, Sugioka Ki, Komori S (2006) New sea spray generation func-
1268 tion for spume droplets. Journal of Geophysical Research: Oceans 111(C2)